TREND

Trapped Radiation Environment Model Development

Technical Note 4

Description of the Combined Release and Radiation Effects Satellite Experiments and Data Sets

ESTEC/Contract No. 9828/92/NL/FM[1]

D. Heynderickx (BIRA/IASB)
J. Lemaire (BIRA/IASB)

November 1992

[1]ESA Technical Management: E.J. Daly (WMA)

Contents

Introduction 1

1 Description of the CRRES experiment 5

1.1 Overview of the CRRES mission 5

1.2 Overview of experiments 6

1.2.1 NASA Chemical Release Experiments 6

1.2.2 DOD Low-Altitude Scientific Studies of Ionospheric Irregularities 10

1.2.3 DOD Studies of the Radiation Environment 10

2 Description of CRRES instruments 15

2.1 Chemical Release Mission 15

2.2 LASSII Experiment 16

2.2.1 Pulsed Plasma Probe 17

2.2.2 Quadrupole Ion Mass Spectrometer 18

2.2.3 Extremely Low Frequency Wave Analyser 18

2.3 Engineering experiments 19

2.3.1 SPACERAD Microelectronics Experiment 19

2.3.2 Internal Discharge Monitor 20

2.3.3 Gallium Arsenide Solar Panel Experiment 21

2.4 SPACERAD Particle Experiments 22

2.4.1 Space Radiation Dosimeter 22

2.4.2 Metal Oxide Semiconductor Dosimeter 23

2.4.3 High Energy Electron Fluxmeter 24

2.4.4 Medium Energy Electron Spectrometer 25

2.4.5 Electron Proton Wide-Angle Spectrometer 27

2.4.6 Low Energy Plasma Analyser 29
2.4.7 Relativistic Proton Detector 30
2.4.8 Proton Switches 30
2.4.9 Proton Telescope 31
2.4.10 Mass Composition Instruments 34
Magnetospheric Ion Composition Spectrometer 35
Low-Energy Magnetospheric Ion Composition Spectrometer 35
Heavy Ion Telescope 36
2.4.11 Spectrometer for Electrons and Protons 36
2.4.12 Low Energy Ion Mass Spectrometer 37
2.4.13 Medium Energy Ion Mass Spectrometer 37
2.4.14 Experiment for High Energy, Heavy Nuclei Composition . 38
2.5 Plasma and Wave Experiments 39
2.5.1 Fluxgate Magnetometer 39
2.5.2 Passive Plasma Sounder and Search Coil Magnetometer . . 40
2.5.3 Electric Field/Langmuir Probe Instrument 41

3 Data availability and quality 43
3.1 The Science Summary Data Base 43
3.1.1 Data format 44
3.1.2 Implementation of ephemeris data 44
3.1.3 Comparison with NASA radiation belt models 49
3.1.4 Location of the South Atlantic Anomaly 49
3.2 The Time History Data Bases 51
3.2.1 Space Radiation Dosimeter 54
3.2.2 High Energy Electron Fluxmeter 55
3.2.3 Medium Energy Electron Spectrometer 57
3.2.4 Electron Proton Angle Spectrometer 61
3.2.5 Proton Telescope 65
3.2.6 Spectrometer for Electrons and Protons 68
3.2.7 Fluxgate Magnetometer 69
3.2.8 Ephemeris data 74
3.2.9 Attitude determination data 78
3.3 Final data sets 78

3.3.1 Preliminary PROTEL data 80
3.3.2 Custom PLGD databases and software 81
DIPOLE DOSE program 82
HE program 82
FLUENCE program 82
DOSE program 82

4 Preliminary results from the CRRES mission **83**
4.1 Magnetic field models 83
4.2 Double-peaked inner radiation belt 85
4.3 Quasi-static model of outer-zone electrons 86
4.4 Development of radiation dose models 87
4.5 Relative position of CRRES and Meteosat 88

References **89**

List of Figures

1 Energy ranges of the electron detectors on CRRES, with their affiliations and calibration facilities. 13

2 Energy ranges of the proton detectors on CRRES, with their affiliations and calibration facilities. 13

3 CRRES altitudes for orbit 250 up to 1500 km derived from Heck's and our version of the interpolated ephemeris. 46

4 Comparison of CRRES perigee altitudes derived from Heck's and our version of the interpolated ephemeris. 47

5 Comparison of CRRES perigee latitudes derived from Heck's and our version of the interpolated ephemeris. 47

6 CRRES altitude for orbit 451 in function of time, for Heck's (dashed line) and our (solid line) version of the ephemeris. 48

7 SSDB differential proton flux at 44.3–53.5 MeV for orbit 451, in function of altitude, for Heck's (dashed line) and our (solid line) version of the ephemeris. 48

8 SSDB differential proton flux at 44.3–53.5 MeV, averaged over orbits 4–463 for altitudes below 1000 km, in function of longitude and latitude (Heck's ephemeris). 50

9 SSDB differential proton flux at 44.3–53.5 MeV, averaged over orbits 4–463 for altitudes below 1000 km, in function of longitude and latitude (our ephemeris). 50

10 SSDB particle fluxes and count rates, averaged over 5° longitude intervals, for orbits 4–463, in function of longitude (our ephemeris). 52

10 (Continued) 53

List of Tables

1	List of CRRES experiments, acronyms, numerical designators and affiliated agencies.	7
1	(Continued)	8
1	(Continued)	9
2	CRRES SPACERAD Particle detector characteristics.	11
2	(Continued)	12
3	Channel response for the MEES detector.	26
4	Channel widths and look directions with respect to the spin axis for EPAS.	28
5	Estimates of the energy ranges and geometric factors for PS.	31
6	PROTEL channel characteristics.	33
7	Record structure of the SSDB header and data records.	45
8	Calibration factors for the Space Radiation Dosimeter.	55
9	Record structure of the HEEF header and data records.	56
10	HEEF Calibration file record structure.	58
11	Record structure of the MEES header and data records.	59
12	MEES Calibration file record structure.	60
13	Record structure of the EPAS header and data records.	62
13	(Continued)	63
14	EPAS Calibration file record structure.	64
15	Record structure of the PROTEL header and data records.	66
16	PROTEL Calibration file record structure.	67
17	Instrument modes for SEP.	68
18	Record structure of the SEP header and data records.	70
18	(Continued)	71
19	Record structure of the Fluxgate Magnetometer header and data records.	72

19 (Continued) 73
19 (Continued) 74
20 Record structure of the ephemeris files. 76
20 (Continued) 77
21 File structure of the attitude coefficient files. 79

Introduction

The Earth's trapped radiation environment is currently described and evaluated, for engineering purposes and spacecraft design, with the empirical NASA/NSSDC trapped radiation model series AP and AE (Vette 1991). The NASA modeling effort covered a period of more than twenty years and incorporated particle data from numerous satellites and instruments in the ensuing models.

The NASA models are issued in the form of tables of the logarithm of the omnidirectional proton or electron flux above various thresholds, in function of McIlwain's (1961) L-parameter and of B/B_0, where B is the value of the geomagnetic field at the specified location, and B_0 is the equatorial field strength of the magnetic field line passing through this location.

Although the NASA models have been very useful in estimating the properties of the trapped particle environment, there is now a wide consensus that they should be replaced by a new generation of particle models, for the following reasons.

1. The NASA models are static. Two versions were released, for conditions of solar minimum and solar maximum, respectively, but effects of variations in the trapped particle environment on shorter time scales can not be evaluated with the current models. Consequently, the NASA models only allow for estimates of the average effect of the trapped radiation for missions of six months or longer.

2. The input to the NASA models consisted of measurements obtained with a variety of detectors, calibration techniques, orbital data, etc., so that the internal consistency and errors are difficult to estimate.

3. Instrument design has advanced enormously over the last decades, so that more accurate and comprehensive measurements are now possible.

4. Several instruments used as input to the NASA models were plagued by severe background contamination, especially electron fluxmeters at low altitudes. In addition, cross-calibration of the various instruments was not always feasible.

5. The measurements were unavoidably contaminated by Starfish and other atmospheric nuclear detonations.

6. Extrapolations were used to model the low- and/or high-energy parts of the particle spectra, both at low altitudes and near the geostationary environment.

7. The NASA models do not contain directional information, since only omnidirectional fluxes are given. In view of describing the low altitude environment, where the East-West asymmetry plays an important role for protons, directional data are needed.

8. The interaction of the Earth's atmosphere with the radiation belts was included as an arbitrary cut-off value for L. New low-altitude models should provide a more realistic description of atmospheric effects.

9. The data were organised in function of a magnetic field model for epoch 1960. The secular variation of the Earth's magnetic field over the period following the development of the NASA models introduces severe difficulties in applying these models to the actual near-Earth environment (Lemaire et al. 1990).

10. No attempt was made to include the contributions of external sources to the geomagnetic field.

11. The organisation of the flux maps in terms of L and B/B_0 introduces large interpolation errors for low altitudes where the particle flux varies rapidly with B/B_0.

The TREND (Trapped Radiation ENvironment Development) study identified specific weaknesses in the existing models and methods and identified suitable satellite data sets for updating the models. TREND recommended the use of the results of the CRRES (Combined Release and Radiation Effects Satellite) mission, in combination with archived data sets, as input for a new modeling effort. In this Technical Note, we review the goals and achievements of the CRRES mission, and describe the various data sets that are available.

In Chapter 1 we describe the orbital characteristics of the CRRES mission, and present an overview of the instrumentation. The detectors are tabulated with their acronyms and experiment number. The energy range of the particle detectors is also given.

Chapter 2 gives a more comprehensive description of the experiments and instruments that make up the CRRES payload. A list of P.I.'s and Co.-I.'s is included.

The availability and format of the data sets that came out of the CRRES experiments and are relevant to the TREND-2 project, form the subject of Chapter 3. The Science Summary Data Base, containing one-minute averages of selected channels

of seven particle detectors and of the magnetic field measurements, is described in Section 3.1. Some preliminary results obtained with this data base are also presented. The Time History Data Bases for the instruments relevant for TREND-2 are discussed in Section 3.2. Section 3.3 contains a description of the final data sets available now or in the near future.

Chapter 4 reviews the preliminary results obtained at PLGD with CRRES data.

Chapter 1

Description of the CRRES experiment

The Combined Release and Radiation Effects Satellite (CRRES) Program is a joint National Aeronautics and Space Administration (NASA) and U.S. Department of Defense (DOD) undertaking to study the near-Earth space environment and the effects of the Earth's radiation environment on state-of-the-art microelectronic components and other spacecraft components.

To perform these studies, CRRES was launched with a complex array of scientific payloads. Among the experiments supported by the CRRES Program, the Phillips Laboratory Geophysics Directorate (formerly AFGL, now PLGD) Space Radiation Effects Program (SPACERAD) is of particular relevance to the TREND-2 study. One of the aims of the SPACERAD Program is to update the static models of the Earth's radiation belts and develop dynamic models of the high-energy particle populations in the near-Earth environment. In addition, radiation-induced single event upsets (SEUs) and total dose degradation of state-of-the-art microelectronics devices are measured in a known space environment.

1.1 Overview of the CRRES mission

The CRRES spacecraft was built by Ball Aerospace Systems Division in Boulder, Colorado under joint sponsorship of NASA and U.S. DOD. The spacecraft was originally built for launch by the Space Shuttle, but was modified for launch on an Atlas-Centaur booster after the Challenger accident.

CRRES was launched on July 25, 1990 at 19h21 UT, into a Geosynchronous Transfer Orbit (GTO) with perigee at 350 km, apogee at 33,500 km, and an inclination of 18.1°. This orbit crosses both the inner and outer radiation belts. The orbital

period is 9^h52^m, and the spin rate is 2 rpm. The spacecraft spin axis is maintained such that the angle between the solar direction and the normal to the top surface, containing solar panels, is always between 5° and 15°.

The spacecraft was designed for a one year mission duration with a goal of 3 years. Unfortunately, due to a battery failure, the mission was aborted on October 9, 1991.

There are three primary mission objectives:

1. to study the effects of the natural radiation environment on microelectronic components and on high-efficiency gallium arsenide solar cells, and to map this environment;
2. to conduct Low-Altitude Satellite Studies of Ionospheric Irregularities (LASSII);
3. to conduct a series of chemical release experiments in the ionosphere and magnetosphere.

Data was recorded on satellite tape recorders continually at 16 kbit/s. The data was transmitted to the ground daily and passed to the data reduction and distribution centre at Hanscom Air Force Base, MA.

1.2 Overview of experiments

In the following sections, we present a brief overview of the experiments that form the payload of CRRES. Although not all experiments are relevant for the TREND-2 study, we present an exhaustive list for the sake of completeness. The instruments are listed in Table 1 with their affiliation, experiment number and acronym.

1.2.1 NASA Chemical Release Experiments

The CRRES payload complement included 24 chemical canisters which were released during the first 13 months of the CRRES mission at altitudes varying from near apogee to near perigee over ground observation sites and diagnostic facilities. These releases formed large clouds of metal vapour, about 100 km in diameter, which interacted with the ionospheric and magnetospheric plasma and the Earth's magnetic field. These releases were studied with optical, radar, and plasma wave and particle instruments from the ground, aircraft, and CRRES.

Table 1. List of CRRES experiments, acronyms, numerical designators and affiliated agencies.

Experiment	Acronym	Designators	Agencies
Microelectronics Test Package	MEP	AFGL-701-1A	**Air Force Phillips Laboratory** Naval Research Laboratory Defense Nuclear Agency Defense Advanced Research Projects Agency Assurance Technology Corporation Telenetics Corporation Fail-Safe Technology Corporation NASA Headquarters NASA Goddard Space Flight Center Microelectronics Working Group Microelectronics Industrial Community
Internal Discharge Monitor	IDM	AFGL-701-1B	**Air Force Phillips Laboratory** Jet Propulsion Laboratory JAYCOR Inc. Beers Associates
Gallium Arsenide Solar Panel Experiment	GASP	AFAPL-801	**Air Force Wright Aeronautical** Hughes Aircraft Company
Space Radiation Dosimeter		AFGL-701-2	**Air Force Phillips Laboratory** Panametrics Inc.
Metal Oxide Semiconductor Dosimeter	MOS	AFGL-701-3	**Naval Research Laboratory**
High Energy Electron Fluxmeter	HEEF	AFGL-701-4	**Air Force Phillips Laboratory** Panametrics Inc.
Medium Energy Electron Spectrometer	MEES, MEA	AFGL-701-5A	**The Aerospace Corporation**
Electron Proton Wide-Angle Spectrometer	EPAS, MEB	AFGL-701-5B	**Max Planck Institut für Aeronomie** The Aerospace Corporation University of Bergen

Table 1. (Continued)

Experiment	Acronym	Designator	Agencies
Low Energy Plasma Analyser	LEPA	AFGL-701-6	**Air Force Phillips Laboratory** Mullard Space Science Laboratory University of Sussex Emmanuel College Amptek Inc.
Relativistic Proton Detector		AFGL-701-7A	**University of California San Diego** The Aerospace Corporation
Proton Switches	PS	AFGL-701-7B	**The Aerospace Corporation**
Proton Telescope	PROTEL	AFGL-701-8&9	**Air Force Phillips Laboratory** Massachusetts Institute of Technology
Magnetosperic Ion Composition Spectrometer	MICS	AFGL-701-11A	**Max Planck Institut für Aeronomie** The Aerospace Corporation University of Bergen Rutherford-Appleton Laboratory
Low-Energy Magnetospheric Ion Composition Spectrometer	LOMICS	AFGL-701-11B	**Los Alamos National Laboratory** The Aerospace Corporation
Heavy Ion Telescope	HIT	AFGL-701-11C	**Los Alamos National Laboratory** The Aerospace Corporation
Fluxgate Magnetometer		AFGL-701-13-1	**Air Force Phillips Laboratory** Schonstedt Instrument Company
Search Coil Magnetometer		AFGL-701-13-2	**University of Iowa**

Table 1. (Continued)

Experiment	Acronym	Designator	Agencies
Electric Field/Langmuir Probe Instrument	EF/LP	AFGL-701-14	**Air Force Phillips Laboratory** University of California Berkeley Regis College Analytyx Electronic Systems Inc. University of California San Diego Cornell University Weitzmann Corporation
Passive Plasma Sounder		AFGL-701-15	**University of Iowa** Fairchild Corporation Analytyx Electronic Systems Inc.
Spectrometer for Electrons and Protons	SEP	ONR-307-3	**Lockheed Palo Alto Research Lab** Office of Naval Research
Low Energy Ion Mass Spectrometer	IMS-LO	ONR-307-8-1&2	**Lockheed Palo Alto Research Lab** Office of Naval Research
Medium Energy Ion Mass Spectrometer	IMS-HI	ONR-307-8-3	**Lockheed Palo Alto Research Lab** Office of Naval Research
Exp. for High Energy, Heavy Nuclei Composition		ONR-604	**University of Chicago** Louisiana State University
Pulsed Plasma Probe	P^3		**Naval Research Laboratory**
Quadrupole Ion Mass Spectrometer	QIMS	NRL-701	**Naval Research Laboratory** Air Force Phillips Laboratory
Extremely Low Frequency Wave Analyser	ELFWA		**Naval Research Laboratory** The Aerospace Corporation
Chemical Release Mission			**NASA MSFC**

1.2.2 DOD Low-Altitude Scientific Studies of Ionospheric Irregularities

LASSII studies naturally occurring and artificially produced ionospheric perturbations and the effects of ionospheric perturbations on communications paths. The LASSII measurements are made near perigee of selected orbits. In addition, LASSII made observations of the low-altitude chemical releases. The onboard set of LASSII instruments consists of two pulsed plasma probes, a very low frequency wave analyser including two electric field antennas and a magnetic hoop antenna, and a quadrupole ion mass spectrometer.

1.2.3 DOD Studies of the Radiation Environment

The primary focus of these studies is on the natural radiation environment and the effects of this environment on microelectronic components. CRRES travels through the inner and outer radiation belts of the Earth, exposing state-of-the-art microelectronic components to this radiation environment to establish their capabilities for use in future space missions. Also, the radiation belts are accurately mapped so that a direct correlation can be made between the exposure and microelectronics performance.

The radiation effects portion of the CRRES mission contains 23 experiments: 3 engineering test packages, 4 field and wave instruments, 14 particle spectrometers and 2 dosimeters.

The particle detectors measure the complete particle spectrum of electrons and protons from a few eV to hundreds of MeV, and heavy ions from about 100 eV/Q up to cosmic ray energies greater than 500 MeV/AMU. Table 2 lists their energy ranges, energy resolution, angular resolution and line of sight. Figures 1 and 2 show the energy overlap and cross-calibration ranges for electrons and ions, respectively. The lower energy particle detectors can produce 3-dimensional distribution functions of both electrons and protons. The instruments are controlled with on-board processors so they can scan in different modes to get the best energy, pitch angle and mass discrimination as the satellite moves from one particle regime to another.

Table 2. CRRES SPACERAD Particle detector characteristics.

Designators	Particles	Energy Range	Energy Resolution	Angular Resolution	Line of Sight
AFGL-701-4 HEEF	electrons	1–10 MeV	10 channels*	±7.5° conical	in spin plane
AFGL-701-5A MEES, MEA	electrons	30 keV – 2 MeV	18 channels*	(±3° – ± 11°) × ±11°	in spin plane
AFGL-701-5B EPAS, MEB	electrons protons	21–285 keV 37 keV – 3.2 MeV	14 channels* 12 channels*	±2.0° × ±3.0° ±2.0° × ±5.0°	25° below spin plane
AFGL-701-6 LEPA	electrons protons	10 eV – 30 keV	3%	±2.8° × ±4.0° standard mode ±2.8° × ±0.5° loss cone mode	in spin plane
AFGL-701-7A	protons	> 320 MeV, > 440 MeV	2 channels		in spin plane
AFGL-701-7B PS	protons	20–80 MeV	20–40 MeV 40–80 MeV	180° conical	in spin plane
AFGL-701-8&9 PROTEL	protons	1–100 MeV	24 channels*	±10° × ±10° low energy ±12° × ±17° high energy	in spin plane

Table 2. (continued)

Designators	Particles	Energy Range	Energy Resolution	Angular Resolution	Line of Sight
AFGL-701-11A MICS	ions	1.2–426.5 keV/Q	< 10%	1° conical	in spin plane
AFGL-701-11B LOMICS	ions	40 eV/Q – 44 keV/Q	7.5%	±6° × 15°	in spin plane
AFGL-701-11C HIT	ions	100 keV/AMU – 15 MeV/AMU	10%	6° conical	in spin plane
ONR-307-3 SEP	electrons protons	20 keV – 5 MeV 500 keV – 100 MeV	24 channels* 48 channels*	6° conical 6° conical	40°, 60°, 80° from spin axis aft
ONR-307-8-1&2 IMS-LO	ions	0.11–35 keV/Q	10%	5° conical	45° & 75° from spin axis aft
ONR-307-8-3 IMS-HI	ions	20–8000 keV/AMU/Q	10%	4° conical	75° from spin axis aft
ONR-604	ions	20 –> 500 MeV/AMU	< 1%	1° conical	in spin plane

*Channel dependent energy resolution

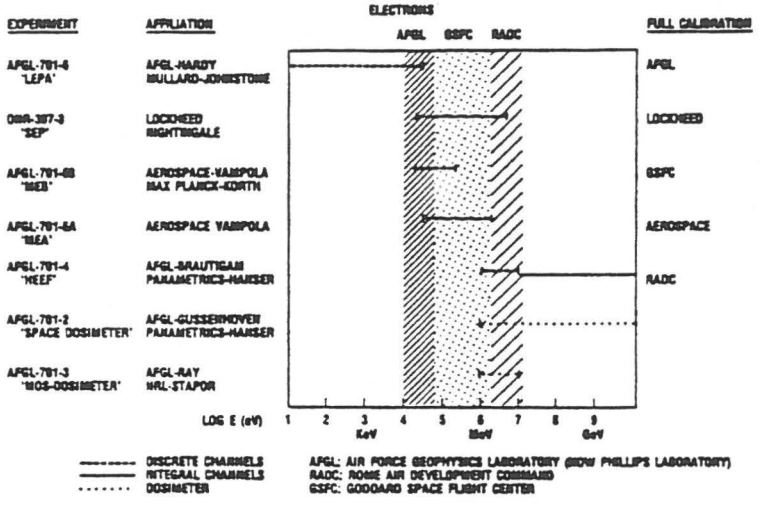

Figure 1. Energy ranges of the electron detectors on CRRES, with their affiliations and calibration facilities. Cross-hatching shows instrument groupings for cross-calibrations at the same facility. [from Mullen & Gussenhoven (1991)]

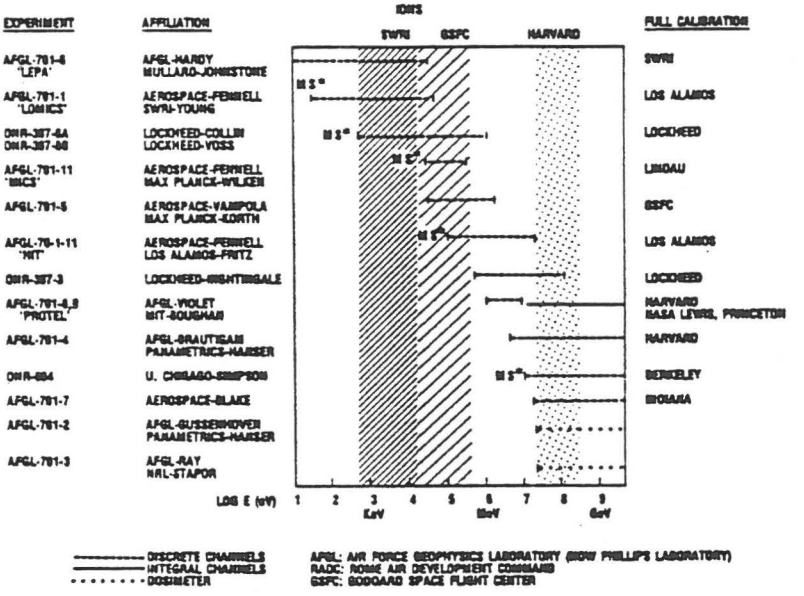

Figure 2. Energy ranges of the proton detectors on CRRES, with their affiliations and calibration facilities. Cross-hatching shows instrument groupings for cross-calibrations at the same facility. MS* designates instruments that differentiate ion mass. [taken from Mullen & Gussenhoven (1991)]

Chapter 2

Description of CRRES instruments

In this chapter we present a brief description of the characteristics and design of the CRRES instruments. Fully detailed technical specifications have been compiled in Gussenhoven et al. (1985), *CRRES System Description Handbook* (1990), TREND TN-6.1, and a series of papers in the July-August 1992 issue of *Journal of Spacecraft and Rockets*.

The TREND-2 study will not make use of all instruments in the CRRES payload. However, since the material we present in this chapter is scattered over several documents and not always consistent, we thought it to be useful to give a more comprehensive description of the CRRES payload than warranted by the TREND-2 study alone. Naturally, the emphasis lies on the experiments to be used as input for TREND-2.

2.1 Chemical Release Mission

P.I.: D.L. Reasoner (NASA MSFC)

The experiments in the chemical release mission on CRRES were motivated by the need to address scientific questions in the areas of coupling between the ionosphere and magnetosphere, response of the magnetosphere system to injections of artificial ion clouds, and instabilities and structuring of the ionosphere in response to perturbations.

CRRES was loaded with over 181 kg of various chemicals, contained in 24 cylindrical canisters which were equally partitioned in two chemical modules. The chemicals contained within the aliminium canisters consisted of a titanium-boron thermite

with barium, lithium, calcium, europium, and/or strontium as the metal to be vaporized.

The releases were studied with optical, radar, and plasma wave and particle instruments from the ground, aircraft, and CRRES. The three chemical release campaigns were:

1. low-altitude releases (near perigee) over the South Pacific in September 1990,
2. high-altitude releases (from about 6000 to about 33500 km) over North America in January and February 1991,
3. low-altitude releases over the Caribbean in July and August 1991.

To accomplish the third chemical release campaign, the orbit apogee was raised by 1450 km using two of the attitude control thrusters. This was accomplished in June 1991 with a series of appropriately timed burns near perigee. An orbit was selected that started with perigee at 314.1° East longitude and drifted 2° westward every 3 days in order for the chemical releases to occur over the Caribbean.

2.2 LASSII Experiment

The objective of the Low-Altitude Scientific Studies of Ionospheric Irregularities (LASSII) experiment is to study plasma irregularities in the ionosphere caused by naturally occurring and artificially created plasma instabilities. Specific investigations include spread-F irregularities, chemical releases, ionospheric modification by intense radio waves, and solar flare disturbances of the ionosphere. These studies will extend the understanding of the effects of ionospheric irregularities on radio-wave propagation in ionospheric ducts, through scintillating regions, and from space-based radars.

LASSII is composed of three space plasma experiments:

1. a Langmuir probe experiment that operates as two pulsed plasma probes (P^3) and is used to measure ionospheric electron densities and temperatures;
2. a quadrupole ion mass spectrometer (QIMS) that is used to measure the densities of positive ions in both the natural ionosphere and in the chemical release experiments;
3. an extremely low frequency wave analyser (ELFWA) that is used to measure the spectrum of both electric and magnetic field fluctuations.

Because the LASSII telemetry format is incompatible with the format used by the wave and particle instruments which are part of the Space Radiation Effects experiment, LASSII is duty cycled using the following scheme. When perigee is between 17h30 and 02h30 LT (i.e. dusk to postmidnight), LASSII operates below 3000 km during every other orbit. When perigee is between 02h30 and 17h30 LT, LASSII operates below 1000 km every fourth orbit. During low-altitude chemical release campaigns, LASSII monitors the ionosphere for four orbits before and after each chemical release.

2.2.1 Pulsed Plasma Probe

P.I.: P. Rodriguez (Naval Research Laboratory)
Co.I.: M.M. Baumback (Naval Research Laboratory)

The Pulsed Plasma Probe (P^3) is used to study plasma irregularities caused by natural perturbations of the ionosphere, and artificial modifications caused by chemical releases from the satellite.

The F-region of the ionosphere is known to exhibit both large-scale and small-scale electron density irregularities, which in some cases can lead to density variations of more than three orders of magnitude. The phenomenon known as spread-F is the most dramatic example of large-scale irregularities occurring at low latitudes. This instability is observed in the nightside of the ionosphere, and is associated with the formation of large-scale density depletions rising to high altitudes from the bottomside of the ionosphere. It is only until CRRES was launched that it has become possible to conduct several different experiments from the same spacecraft to compare naturally occurring instabilities with artificial electron density irregularities created by chemical releases.

The P^3 is designed to measure the electron density and temperature, and fluctuations of the ambient ionospheric plasma. The experiment consists of two cylindrical Langmuir probes, two preamplifiers, and a main electronics box. Each of the Langmuir probes is made of tungsten wire 20 cm long and 0.09 cm in diameter, mounted on the end of a boom about 2 m in length. The booms are deployed opposite each other at a 45° angle to the plane of the solar panels.

2.2.2 Quadrupole Ion Mass Spectrometer

NRL-701

P.I.: P. Rodriguez (Naval Research Laboratory)
Co.I.: D.E. Hunton (PLGD)

The Quadrupole Ion Mass Spectrometer (QIMS) measures the identities and relative concentrations of ionospheric positive ions, both ambient and those produced by photo-ionization of the released chemicals. The mass spectrometer is designed to be sensitive to thermal ions in the stationary ionosphere and to the ions formed following chemical releases. These ions have energies in the range of 0–100 eV in the instrument's frame of reference. This is a very different operation regime than the other ion mass spectrometers onboard CRRES.

The mass range of the spectrometer is 4–155 AMU. All ambient ions (with the exception of H^+) and all ions derived from the chemical releases fall into this range. The resolution of the instrument was adjusted to give the mass peaks a full width at half-maximum of ~ 2 amu across the entire mass range. This is sufficient resolution to separate the two O^+ isotopes at masses 16 and 18, to separate the ambient molecular ions at masses 28, 30, and 32, and to differentiate between all of the metal ions (Li^+, Sr^+, Ca^+, Ba^+, and Eu^+) derived from the chemical releases. Because the total ion density is measured by the aperture plate and the LASSII P^3 Langmuir probe, a very high sensitivity for the instrument was chosen during calibration to maximize detection of trace species.

2.2.3 Extremely Low Frequency Wave Analyser

P.I.: P. Rodriguez (Naval Research Laboratory)
Co.I.: H.C. Koons (The Aerospace Corporation)

The Extremely Low Frequency Wave Analyser (ELFWA) instrument measures electrostatic and electromagnetic ion waves in the ambient ionosphere and during active experiments involving chemical releases and the ionospheric heater at Arecibo, Puerto Rico. It also measures long-wavelength (> 100 m) electron density irregularities. These irregularities degrade communication, navigation, and radar signals that propagate through the ionosphere.

The ELFWA measures single-axis electric field spectra and amplitudes from 10 to 250 Hz and single-axis magnetic field spectra and amplitudes from 10 to 125 Hz. The instrument consists of two antennas, two preamplifiers, and two electronics boxes. The electric field antenna consists of two spherical probes, each 6.35 cm in diameter, deployed on booms 190.5 cm long above the spacecraft. The signals from the two probes are differenced in the E-field electronics package to provide a

single-axis measurement of the electric field in the spin plane of the spacecraft. The magnetic field antenna is a 50 cm diameter, 1600-turn loop of AWG36 copper wire, deployed on a 2 m boom. The single-axis magnetic field measurement is also made in the spin plane of the spacecraft. The two electronics packages, E-field and B-field, condition the antenna signals for data storage and telemetry.

At perigee, the spectrum detected by both antennas is characterized by electromagnetic impulses across the entire frequency range from 10 to 250 Hz. These impulses are most likely generated by lightning. At higher altitudes, there is a hiss-like spectrum extending from 50 Hz to above the bandpass of the analyser. This may be the lowest spectral component of plasmaspheric hiss.

2.3 Engineering experiments

High energy particles can degrade the performance of spacecraft in several ways. Three engineering experiments are flown on CRRES to measure deleterious effects of the harsh near-Earth high energy particle environment. The three experiments are the MicroElectronics Package (MEP), the Internal Discharge Monitor (IDM), and the Gallium Arsenide (GaAs) Solar Cell Panel (GASP) Experiment.

The MEP measures Single Event Upsets (SEUs), total dose, and dose rate effects on advanced technology microelectronics devices. The IDM measures arc discharges caused by deep dielectric charging in semiconductor materials typically used in or on operational spacecraft. The Solar Cell Experiment measures the performance characteristics of advanced GaAs solar cells as they degrade in the radiation environment.

2.3.1 SPACERAD Microelectronics Experiment

AFGL-701-1A
P.I.: E.G. Mullen (PLGD)

The purpose of the SPACERAD Microelectronics Experiment is to study radiation induced SEUs and total dose damage in advanced microelectronic devices in the measured space environment and at particle accelerators. The space experiment monitors the operations of state-of-the-art silicon devices, VHSIC (Very High Speed Integrated Circuit) devices, and advanced material devices such as gallium arsenide (GaAs) random access memories (RAMs). The devices have been selected because of their present and proposed use in DOD and NASA space programs and their scientific interest, such as comparison of feature sizes, technologies, materials, etc. . The space experiment is complemented by ground test and device modeling programs to provide a direct comparison of their data with space measurements.

Ground testing of devices from the same lot and wafer (when available) were used in conjunction with present radiation belt and device models to predict, prior to flight, the expected SEUs in space.

The satellite contains a complete set of particle instruments to measure simultaneously the cosmic rays, high energy protons, and high energy electrons in the space environment. Thus, the SEUs and the total-dose damage will be directly related to the particle environments producing them. Space results will check model predictions and determine the validity of ground test procedures and existing device models.

The Microelectronics Test Package (MEP), the flight package of the Microelectronics Experiment program, has two broad measurement areas: (1) SEUs in selected memory, microprocessor, and VHSIC devices, and (2) parameter shifts caused by accumulated total radiation dose in the memory, microprocessor, and VHSIC devices, as well as in inverters, operational amplifiers, comparators, A/D convertors, and discrete transistors.

Semiconductor dosimeters are distributed throughout the MEP to measure the radiation exposure accumulated in flight on the circuit boards where the microelectronics test devices are mounted. Temperature sensors are also mounted on the test circuit boards to help differentiate between radiation effects and normal parameter shifts induced by temperature changes. Silicon and GaAs thin barrier radiation detectors with associated linear amplifiers and pulse height analysers are also in the MEP to measure the energy spectrum of the radiation environment as seen by the devices under test.

Approximately 65 device types and over 450 devices are space tested. The memory devices include GaAs RAMs, CMOS and MNOS PROMS, and CMOS and CMOS/SOS gate arrays. The microprocessor test candidates include both CMOS and bipolar types. The inverters are CMOS. The op amps and comparators are bipolar. The A/D convertors are both CMOS and bipolar. The discrete transistors and semiconductor dosimeters are CMOS.

2.3.2 Internal Discharge Monitor

AFGL-701-1B

P.I.: R. Fredricksson (RADC)

The objective of the Internal Discharge Monitor (IDM) experiment is to characterize internal electrostatic discharge events that may damage or upset (disturb) electronic circuits in spacecraft subjected to high energy charged particle radiation environments. The IDM experiment is part of the Air Force Weapons Laboratory (AFWL) on-going Electron-Caused ElectroMagnetic Pulse (ECEMP) effort. The IDM exper-

iment is designed to determine whether or not internal discharge phenomena indeed occur under the CRRES orbital conditions, and, if so, to measure the characteristics of the discharge.

The IDM instrument tests 16 dielectric samples. The dielectric materials and geometric configurations were selected after ground tests in which samples were irradiated with 1 to 3 MeV electrons in the JPL dynamitron. The experiment data will be correlated with the orbital environment to determine the quantitative dependence of the discharge phenomena on the ionizing radiation flux and spectrum, and on material properties.

2.3.3 Gallium Arsenide Solar Panel Experiment

AFAPL-801

P.I.: T.M. Trumble (Air Force Wright Aeronautical Laboratories)

The five major objectives of the Gallium Arsenide Solar Panel (GASP) experiment are:

1. to measure in the space environment the performance characteristics of differently configured advanced solar cell strings while measuring the radiation species (protons, electrons, ions), their flux levels, and their energy distribution;

2. to quantify radiation damage of GaAs and advanced silicon solar cells;

3. to select the optimum method (continuous heating, forward current bias heating, or intermittent heating) for annealing radiation damaged cells;

4. to determine optimum panel annealing parameters and operating characteristics;

5. to determine the optimum configuration for solar cell panels operating in a high radiation environment.

GASP will evaluate and improve radiation damage models of GaAs solar cells and will make significant contributions to the JPL Solar Cell Radiation Handbook. The radiation damage model portion of this experiment depends heavily on the success of the high energy particle measurement experiments on board the CRRES satellite.

2.4 SPACERAD Particle Experiments

The SPACERAD particle detectors were designed to give measurements with high time, angular, and energy resolution of electrons (10 eV to 10 MeV), protons (10 eV to 600 MeV), and the major ion species (40 eV/Q to 15 MeV/ion). Additional information is provided by supporting experiments from the Lockheed Electron and Proton Spectrometer and Mass Composition Experiments, and the University of Chicago Cosmic Ray Experiment. In addition, SPACERAD will provide dose measurements by two very different methods.

The data from these experiments are used to:

1. provide concurrent environmental specifications for the Engineering Experiments, particularly for the Microelectronics Experiment;
2. extend existing static radiation belt models in energy, pitch angle, and ion composition;
3. study in detail the dynamic processes of the radiation belts.

2.4.1 Space Radiation Dosimeter

AFGL-701-2

P.I.: E.G. Mullen (PLGD)
Co.-I.: M.S. Gussenhoven (PLGD)
F. Hanser (Panametrics)
B. Dichter (Panametrics)

The primary purpose of the Space Radiation Dosimeter is to measure the radiation dose from both electrons and protons as well as the number of nuclear star events occurring behind four different thicknesses of aluminium shielding. In addition, it provides some information on the integral flux of electrons and protons at energies above the thresholds defined by the shields. The experiment will provide information on the relationship between the flux of high energy particles incident to the spacecraft and the actual radiation dose to which microelectronic components are exposed. This information is necessary for determining the relationship between variations in the Earth's radiation belts and the behaviour and lifetime of microelectronic components.

The instrument contains four sensors, with the active measuring device being a p-i-n diffused junction silicon semiconductor with a guard ring. Each device is mounted behind a hemispherical aluminium shield. The aliminium shields are chosen to provide electron energy thresholds for the four sensors of 1, 2.5, 5 and 10 MeV, and for protons of 20, 35, 51 and 75 MeV. The 1 MeV threshold sensor has a detector

area of 0.051 cm^2, and the remaining three each have areas of 1.00 cm^2. Particles that penetrate the shield and bremsstrahlung produced in the shield that impact the active element will both deposit energy in the device, producing a charge pulse. The charge pulse is shaped and amplified. The pulse height is proportional to the energy deposition in the detector.

Energy depositions between 50 keV and 1 MeV are summed to give the low linear energy transfer (LOLET) dose. Depositions between 1 MeV and 10 MeV are summed to give the high linear energy transfer (HILET) dose. Depositions above $\sim$ 40 MeV are counted as very high linear energy transfer (VHLET) events. The LOLET dose comes primarily from electrons, high energy protons (above 100-200 MeV), and bremsstrahlung. The HILET dose is primarily from protons below 100–200 MeV. The VHLET dose comes from nuclear star interactions of high energy protons, from heavier cosmic rays, and from the very small percentage of trapped radiation particles that have long path lengths in the detectors.

The dose is taken to be directly proportional to the total energy deposited in the detector. Each pulse is analysed to determine whether it will be counted for electron or proton dose or a nuclear star event. The pulse height is then digitized and added to the sum of all other pulse heights measured in the accumulation interval. In addition, the total number of pulses measured in the accumulation interval is also recorded for both electrons and ions. Without significant bremsstrahlung, this number of counts should be directly proportional to the integral flux of electrons and ions above the threshold produced by the aluminium shield.

The two lowest threshold detectors should provide both good flux and dose determinations, while the two remaining detectors provide primarily dose data.

2.4.2 Metal Oxide Semiconductor Dosimeter

AFGL-701-3

P.I.: E.G. Mullen (PLGD)
Co.-I.: B. Stapor (Naval Research Laboratory)

The objective of the Metal Oxide Semiconductor (MOS) Dosimeter is to measure integrated dose as a function of depth in aluminium. Radiation soft PMOS transistors are placed beneath various thicknesses of aluminium to get the desired dose-depth curve. The integrated dose is determined by measuring the shift in transistor threshold voltage. The relationship between shift in threshold voltage and integrated dose is determined with a calibrated radiation source, usually Co-60 γ rays.

In the package flown, four sensors (PMOS transistors) are operated at positive gate biases. By using different thicknesses of aluminium above the sensors, a measure of the integrated doses caused primarily by electrons and protons at different depths

is obtainable. This information is of substantial interest since even radiation soft devices flown in space survive for much longer than is predicted from laboratory experiments and from the integrated dose predictions of the currently accepted space radiation models.

The integrated dose resulting primarily from electrons and protons can be compared with the calculations based on the currently employed space radiation models and the models to be developed based on the SPACERAD results. These results can also be compared with the results from the Space Radiation Dosimeter.

2.4.3 High Energy Electron Fluxmeter

AFGL-701-4

P.I.: E.G. Mullen (PLGD)
Co.-I.: D. Brautigam (PLGD)
F. Hanser (Panametrics)
B. Dichter (Panametrics)

The High Energy Electron Fluxmeter (HEEF) is a solid state spectrometer telescope designed to measure differential electron energy spectra in 10 energy channels from 1 to 10 MeV. Electrons in this energy range are the source of a significant portion of the total radiation dose received by microelectronic components in space systems operating in the Earth's radiation belts. Determining the average value and dynamic behaviour of these electrons is critical to the CRRES program.

The instrument is of a telescopic design with two solid state detectors stacked in front of a BGO scintillating crystal. In order to be counted, an electron must produce a triple coincidence of pulses in the two solid state detectors and the BGO crystal, and have an anticoincidence with particles detected in the annular plastic scintillator surrounding the BGO crystal. Each electron between 1 and 10 MeV that enters the detector through the aperture produces pulses in the two solid state detectors and photons in the BGO crystal. The photons produced in the crystal are seen by a photomultiplier tube, optically coupled to the crystal. The photomultiplier tube produces charge pulses proportional to the number of photons seen. The charge pulses seen in coincidence are all pulse-shaped in a shaping circuit. If the three pulses all fall within the proper broad pulse height range, the BGO crystal pulses are further analysed in a pulse height analyser and placed into the proper energy electron counter bin for transfer to shift registers for satellite readout. The registers are read every 0.5 s and stored by the satellite data storage and telemetry system, resulting in a data base of 2 measurements per second per channel.

The largest problem with measuring MeV electrons, especially in the CRRES orbit, is contamination due to high energy protons and bremsstrahlung. Great care was taken in the detector design to try and eliminate all counts other than

the 1–10 MeV electrons which directly enter the aperture. Protons that come directly down the aperture are not counted because they have excessive energy loss in the solid state detectors (for protons with energies less than 100 MeV) or in the BGO crystal (for protons with energies greater than 30 MeV). For particles which can penetrate the heavy shielding (greater than 140 MeV protons and greater than 20 MeV electrons), the annular plastic scintillator produces anticoincidence counts which reject the particles being counted. A 0.006 in beryllium foil stops electrons with energies less than 140 keV that directly enter the aperture. The tungsten collimators and shield reduce bremsstrahlung, and the magnesium housing reduces bremsstrahlung production from less than 10 MeV electrons. The detector rejection of unwanted particles seems to have worked extremely well in that the data taken on orbit have been remarkably free of background contamination.

2.4.4 Medium Energy Electron Spectrometer

AFGL-701-5A

P.I.: E.G. Mullen (PLGD)
Co.-I.: A. Vampola (The Aerospace Corporation)

The Medium Energy Electron Spectrometer (MEES), also called Magnetic Electron Spectrometer (MEA), uses the principle of momentum analysis in a solenoidal magnetic field. In a 180° magnetic electron spectrometer, particles entering an aperture encounter a uniform solenoidal magnetic field and travel a circular path in the plane transverse to the field. After being bent through approximately 180°, the particle is detected by a planar array. First order focusing occurs in the plane. Electrons with the same energy, although at different angles, are focused on almost the same vertical line on the detection plane. There is no focusing in the vertical direction.

At the 180° focus, the electrons impinge upon a detector array consisting of six ion-implanted silicon plates mounted in three pairs on a thick circuit card. There are a total of 18 detection areas in the array. Generation of a particle count is initiated by an electron impinging on a detector configured as a reverse-biased P-N diode and depositing most or all of its energy as charge pairs, at a rate of 3.6 eV/pair, in the depletion region of the N-type silicon. The charge pairs are swept out of the depletion region by the biasing network, creating a charge pulse which is proportional to the energy of the incident electron minus energy lost as bremsstrahlung or residual electron energy (the electrons which may backscatter out of the detector).

Pulses with amplitudes below the lower discriminator threshold are considered noise or bremsstrahlung and are rejected. Pulses with amplitude above the upper discriminator threshold are due to highly ionizing particles (or long path length trajectories of very energetic particles) and are rejected as unwanted background.

Table 3. Channel response for the MEES detector [from Vampola et al. (1992)]. Column 1 contains the channel number, columns 2 and 3 the nominal lower and upper energy bounds, column 4 gives the centre of response (E_c), column 5 the geometric-energy factor (GEF), and column 6 the actual channel limiting angle. Energies are given in keV, the GEF are in units of (cm^2 s sr keV).

Channel	E_{min}	E_{max}	E_c	GEF	Angle
0	110	188	153	5.88	8.24
1	174	257	214	5.68	6.37
2	230	314	271	5.16	5.19
3	297	384	340	4.84	4.38
4	374	462	418	4.59	3.78
5	465	553	510	4.19	3.24
6	558	649	604	3.89	2.90
7	646	738	693	3.58	2.63
8	735	829	782	3.30	2.40
9	828	923	876	3.08	2.21
10	928	1024	976	2.89	2.05
11	1042	1139	1090	2.66	1.88
12	1131	1227	1178	2.49	1.76
13	1239	1337	1287	2.37	1.66
14	1322	1419	1370	2.23	1.56
15	1423	1520	1470	2.14	1.48
16			background		
17	1534	1633	1582	2.03	1.41

The low threshold ensures efficient detection of electrons which backscatter out of a detector after depositing only part of their energy. The upper threshold ensures detection of valid events in the presence of noise or low-energy bremsstrahlung which add to the pulse height. For more energetic electrons, the lower threshold is set at the energy corresponding to a minimum ionizing particle traversing a minimal path through the detector (400 keV). This assures efficient detection of energetic electrons that pass through the detector with little scattering.

Table 3 provides a list of the nominal energy boundaries, centre of response, geometric-energy factor (GEF), and actual channel limiting angle in the spin plane, for each detector channel. The nominal energy boundaries contain more than 90% of the total response in a channel. The centre of response is defined so that 50% of the GEF is above and 50% below this value. The peak response of the channel is very close to this value (within 1 or 2%). The GEFs are based on the laboratory

calibration data obtained just prior to final delivery in January, 1990. For the transformation to flux, counts/s must be divided by the GEF. Note that the counts in the data stream are counts per 0.512 s.

The narrow acceptance angle in the spin plane provides very good pitch angle resolution, especially at high energy. The full field of view, coupled with the angular scan of 6° which occurs during the 0.512 s data accumulation period, results in a total acceptance angle within a single data sample of about 8–18°, depending on channel. The true pitch angle distribution of the particles can be established to about 0.5° through a deconvolution procedure which is limited by the accuracy of the onboard magnetometer data and by the statistics of the counts in the samples.

2.4.5 Electron Proton Wide-Angle Spectrometer

AFGL-701-5B
P.I.: E.G. Mullen (PLGD)
Co.-I.: A. Korth (Max Planck)

The Electron and Proton Wide-Angle Spectrometer (EPAS, MEB) measures protons and electrons with emphasis on wide pitch angle coverage with good pitch angle resolution. EPAS consists of two identical units to measure electrons simultaneously in ten directions and ions in four directions over a total angular range of $\sim 110°$.

Each unit contains a magnetic deflection system and an array of solid-state detectors. Particles entering the spectrometer encounter a homogeneous magnetic field of 0.08 T which separates protons and heavier ions from electrons. The magnetic field geometry was designed such that a parallel beam of electrons entering the instrument at a given angle with respect to the axis of the aperture is deflected and focused to a single point irrespective of its energy. The deflection system thus defines a focal curve on which each point corresponds to a given angle of incidence to the spectrometer. Along this focal curve, five rectangular solid-state detectors are mounted which define five angular intervals within the 60° aperture of the unit. The focusing can be achieved for electrons with energies between 15 and 300 keV. The total energy range of the detectors is divided into 14 approximately logarithmically spaced energy channels that are called differential energy channels. The channel widths and look directions of the electron detectors are listed in Table 4.

The deflection of ions with energies above 20 keV is negligible. They move on almost straight lines and are detected in solid-state detector telescopes. For each unit, two telescopes are mounted behind the magnetic deflection system, defining two directions for the measurement of ions. Each telescope consists of a front and a back solid-state detector. The front detector is used for the energy analysis of ions, the back detector provides a veto signal to reject penetrating particles. The total energy

Table 4. Channel widths and look directions with respect to the spin axis for EPAS [from Korth et al. (1992)].

Channel	Channel width	Detector	Look direction
	Electrons		
1	21.0–31.5 keV	E0	20°
2	31.5–40.0 keV	E1	30°
3	40.0–49.5 keV	E2	40°
4	49.5–59.0 keV	E3	50°
5	59.0–69.0 keV	E4	60°
6	69.0–81.0 keV	E5	70°
7	81.0–94.5 keV	E6	80°
8	94.5–112.0 keV	E7	90°
9	112.0–129.5 keV	E8	100°
10	129.5–151.0 keV	E9	110°
11	151.0–177.5 keV		
12	177.5–208.0 keV		
13	208.0–242.5 keV		
14	242.5–285.0 keV		
	Protons		
1	37–54 keV	P0	26°
2	54–69 keV	P1	46°
3	69–85 keV	P2	87°
4	85–113 keV	P3	107°
5	113–147 keV		
6	147–193 keV		
7	193–254 keV		
8	254–335 keV		
9	335–447 keV		
10	447–602 keV		
11	602–805 keV		
12	805–3200 keV		

range is divided into 12 approximately logarithmically spaced energy channels, which are listed in Table 4, together with the look directions of the telescopes.

Because of the deflection in the magnetic field, electrons with energies below 800 keV cannot reach the proton telescopes. Electrons with higher energies penetrate the front detector, provide a veto signal in the back detector, and are rejected. For this reason, the lowest energy threshold for the protons is essentially given by the noise of the front detector and the analog electronics.

The EPAS spectrometer contains two of the described units and covers in total an angular range of $\sim 110°$. The sensor is mounted on the platform of the spacecraft and is directed such that the angular range of 110° is located in the meridian plane of the satellite. The spin axis of the spacecraft is located in the orbital plane.

2.4.6 Low Energy Plasma Analyser

AFGL-701-6

P.I.: E.G. Mullen (PLGD)
Co.-I.: D. Hardy (PLGD)
A. Johnstone (MSSL)
P. Gough (Sussex University)

The Low Energy Plasma Analyser (LEPA) for CRRES is designed to measure the three-dimensional distribution function of electrons and ions in the energy range 10 eV – 30 keV and to determine where in the distribution function and at what frequency coherent wave-particle interactions occur.

LEPA belongs to a new class of particle experiments designed to make increasingly sophisticated, simultaneous, multi-angular measurements. These detectors have been capable of making true measurements of the three-dimensional distribution function. For LEPA, particles are measured within a field-of-view of $120° \times 5.6°$ with the instrument mounted on the satellite such that the 120° fan is in a meridian plane relative to the spin axis of the satellite and centred on the satellite's equator. The instrument can resolve the direction of arrival of particles in this angular range to within approximately 1°. As the spacecraft rotates, the sensor sweeps out approximately 90% of the full solid angle of 4π. Under almost all circumstances, this solid angle includes the directions parallel and anti-parallel to the magnetic field, allowing the flux at all pitch angles to be sampled. LEPA is the first instrument to explore the inner magnetospheric region with the capability of routinely monitoring the full pitch angle distribution from 0° to 180° with a resolution of the order of 1°.

A particle correlator was developed as an integral part of LEPA. The particle correlator technique provides a direct method of identifying regions of particle velocity space in which strong wave-particle interactions occur. This is done by analysing

in real-time, within the instrument, the time series of pulses from the particle detector, within the detector sampling interval, at a given energy and pitch angle. Autocorrelation functions of the time series are calculated, and the arrays of autocorrelation functions vs. energy and pitch angle are accumulated in a way suitable for the available telemetry. In post-processing on the ground, the autocorrelation function arrays are searched for periodic or transient features with wave activity, boundary crossings, and special events.

The LEPA particle correlator operates also in a novel direct wave-particle mode, in which waves (below 30 kHz), measured by separate on-board electric field and wave experiments, and LEPA signals are directly cross-correlated on board. The correlator searches for correlations in the frequency range 0–4.5 kHz while the LEPA instrument is measuring both ions and electrons from a few eV to 30 keV. This mode is intended to study the electron cyclotron mode at low gyroharmonics and ion waves at low frequencies.

2.4.7 Relativistic Proton Detector

AFGL-701-7A

P.I.: E.G. Mullen (PLGD)
Co.-I.: A. Kolasinski (The Aerospace Corporation)

The immediate objective of the Relativistic Proton Detector is to measure the energy spectra and pitch angle distribution of relativistic protons trapped in the inner Van Allen belt.

The primary sensor is a Cerenkov radiator viewed by a photomultiplier tube. Two copies of this sensor with different radiators respond to protons with energies above 440 MeV and 320 MeV, respectively. An additional system measures electrons and consists of two detectors: an electron scatter detector for electrons with energies above 200 keV, and a heavily shielded minimum-ionizing detector for penetrating electrons (> 35 MeV) and protons (> 80 MeV). Finally, a photometer system was included to view the GTO chemical releases. The photometer measures narrow-band emissions from lithium, barium, and europium in four wavelength regions simultaneously using a split-anode microchannel plate photomultiplier tube.

2.4.8 Proton Switches

AFGL-701-7B

P.I.: E.G. Mullen (PLGD)
Co.-I.: J.B. Blake (The Aerospace Corporation)

The Proton Switches (PS) are two omnidirectional detectors, sensitive to protons

Table 5. Estimates of the energy ranges and geometric factors for PS [from Blake & Imamoto (1992)].

Channel	Energy range (MeV)	Geometric factor (mm^2)
PS2L	21–84	3.9
PS2H	23–51	2.6
PS1L	51–107	3.6
PS1H	51–77	2.7

(and heavier ions). The purpose of the PS is to signal the data processing unit (DPU) when energetic protons are present so that the DPU can modify the telemetry allocation among the various Aerospace sensors.

The PS detectors are Li-drifted silicon with a cubical shape, 3 mm on an edge. A uniform hemispherical shield is placed over the upper 2π solid angle. The rear 2π solid angle is shielded far more massively. The discriminator levels are chosen to be several times the energy which an electron can deposit in the detector. As a result, only protons and heavier ions are detected, and background caused by electron pileup is nil. The sensors show a very low count rate due to galactic cosmic rays. Since there are very few cosmic rays in the passbands of the proton switches, the major causes of these background counts are nuclear interactions in the detector itself and neutron-induced reactions in the detector where the neutrons are secondaries generated in the spacecraft. The energy thresholds were chosen to be 20 MeV and 50 MeV (for protons).

A zeroth-order estimate of the geometric factor has been computed with the assumption that the spectral shape is exponential and fixed over the entire energy range of integration. The resulting geometric factors are tabulated in Table 5, but should be used with care as they are rough approximations.

2.4.9 Proton Telescope

AFGL-701-8&9

P.I.: E.G. Mullen (PLGD)
Co.-I.: M. Violet (PLGD)
M.S. Gussenhoven (PLGD)

The objective of the Proton Telescope (PROTEL) is to make well calibrated, high resolution measurements of the differential energy spectrum of protons in 24 channels spaced logarithmically from 1 to 100 MeV. PROTEL consists of two solid state

detector assemblies (sensors) and a data processing unit (DPU). The Low Energy sensor Head (LEH) measures 1–9 MeV protons in 8 contiguous energy channels. The High Energy sensor Head (HEH) measures 6–100 MeV protons in 16 contiguous energy channels. The entire 24 point spectrum is returned once per second.

The two sensors consist of a stack of silicon solid-state detectors in a shielded assembly that have to satisfy certain coincidence/anticoincidence conditions to produce particle counts. Contamination from high energy protons presents the biggest problem in producing an accurate data set. In order to minimize contamination, each sensor has a collimator, a sweeping magnet, and passive and active shielding to reduce unwanted particles. In addition, the high energy sensor also has active anticoincidence rejection via guard rings around the silicon-lithium detectors.

The aluminium collimator reduces the proton and electron fluxes from outside of the acceptance cone. PROTEL shields out electrons very effectively. The passive shielding around the detector stack has a range of 50 MeV for orthogonally impinging electrons. Protons outside of the acceptance cone whose trajectories through the detector stack could cause a false count are shielded from energies below 195 MeV to 289 MeV depending on the channel and the incoming proton's position and angle. The inside surface of the collimator has a saw-toothed pattern to reduce the forward scattering of particles into the entrance aperture, and is painted with a conductive matte black paint to minimize light scattering towards the detectors. Electrons can produce an enhanced background noise count and are diverted from the detectors by the sweeping magnet.

Both surface barrier and lithium-drifted silicon detectors are used in PROTEL. The LEH uses 5 surface barrier detectors and the HEH uses a front surface barrier detector followed by a stack of 5 lithium-drifted silicon detectors. In the LEH (HEH) the first 4 (5) detectors determine the incoming proton energy. The 5^{th} (6^{th}) detector, separated from the rest by an aluminium (brass) absorber, is operated in anticoincidence with the rest, defining an upper threshold of 9 (100) MeV. The first five detectors of the HEH also have active shielding in the form of an anticoincidence ring. The ring is part of the same silicon wafer as the detecting element, but is electrically isolated, creating a second 'detector' outside the acceptance angle. Pulses in the detector stack which are coincident with pulses in the rings are rejected in order to reduce background counts produced by penetrating particles.

A proton which passes within the acceptance cone defined by the collimator of one of the sensor heads enters the detector stack where it either loses all or a portion of its energy. The amount of energy deposited in each detector is analysed by the system logic, which determines if detectors were triggered within a fixed time window (2.0 μs, LEH; 0.5 μs, HEH). The system then evaluates the energy deposited in each triggered detector to determine in which channel, if any, to record the particle.

The instrument was calibrated at three proton accelerator beam facilities with

Table 6. PROTEL channel characteristics [from Violet et al. (1992)].

Channel	Energy Range (MeV)	E_{avg} (MeV)	E_{peak} (MeV)	Conversion factor $1/G$ $(cm^2\,s\,sr\,MeV)^{-1}$
		High Energy Head		
1	6.0–7.7	6.8	6.8	5.6
2	7.5–9.6	8.5	8.5	4.5
3	9.3–10.2	9.7	9.7	17.2
4	9.9–11.5	10.7	10.5	8.2
5	11.2–15.2	13.2	13.0	3.1
6	14.7–15.9	15.2	15.1	19.8
7	15.5–18.3	16.9	16.2	3.8
8	18.0–20.8	19.4	19.4	1.7
9	25.3–27.2	26.3	26.3	5.9
10	26.1–35.6	30.9	30.8	1.5
11	34.9–37.7	36.3	36.3	6.6
12	37.8–48.1	42.3	41.3	0.9
13	44.3–53.5	47.5	45.7	1.5
14	53.5–62.1	57.0	55.4	1.5
15	62.1–73.1	67.5	66.9	1.5
16	73.1–100.0	82.9	77.3	0.6
		Low Energy Head		
1	1.0–2.1	1.5	1.5	85.1
2	2.0–2.3	2.1	2.1	903.4
3	2.2–2.8	2.5	2.4	299.2
4	2.8–3.2	2.9	2.9	1279.7
5	3.1–4.1	3.6	3.6	135.8
6	3.9–4.8	4.3	4.2	156.1
7	4.6–7.0	5.7	5.0	99.2
8	7.3–9.4	8.4	8.6	435.1

energies ranging from 1.5 MeV to 159 MeV. The resulting channel boundaries and conversion factors for both sensors are listed in Table 6. The differential energy flux J, in protons/(cm^2 s sr MeV), is given by

$$J = \frac{\text{COUNTS}}{G\,\Delta t \int_{E_L}^{E_U} \epsilon(E)\,dE},$$

where G is the geometric factor, E_L and E_U are the channel boundaries, $\epsilon(E)$ is the energy-dependent efficiency, and Δt is the accumulation time of the instrument (1.0236 s).

For the best part of the CRRES orbit the shielding and anticoincidence rejection work very well, but contamination levels can become significant at the inner edge of the inner proton belt, where high fluxes occur of particles with energies higher than 100 MeV. These high-energy particles can penetrate detector shieldings and produce false counts at lower energies. The contamination levels can be estimated by modeling the contamination of the detector. The first steps included measuring the response of the HEH to $>$ 100 MeV proton beams at various angles outside the detector acceptance cone and calculating the energy loss in various directions using a simplified materials model of the instrument. This led to the development of the PROTEL Contamination Code which computes counts that would be recorded in the HEH using a Monte Carlo integration approach and the Janni energy range tables. Both nominal performance and contamination are modeled. Indications from the model and early data are that the effects are minor and can be corrected for in the data analysis process.

2.4.10 Mass Composition Instruments

The objective of the Mass Composition Instruments is the unambiguous determination of the composition of the plasma and energetic particle populations of the Earth's trapped radiation belts over the range of 40 eV/Q to 15 MeV per ion to identify mechanisms that energize charged particles and transport them from their parent source populations to the magnetosphere.

The Mass Composition Instruments incorporate three types of sensor systems: the Low-Energy Magnetospheric Ion Composition Spectrometer (LOMICS), the Magnetospheric Ion Composition Spectrometer (MICS), and the Heavy Ion Telescope (HIT). Each of these performs a multiple-parameter measurement of the composition of magnetospherically trapped and transient ion populations over a combined energy range from 40 eV/Q to 15 MeV per ion and for elements from hydrogen through iron.

Magnetospheric Ion Composition Spectrometer

AFGL-701-11A
P.I.: E.G. Mullen (PLGD)
Co.-I.: B. Wilken (Max Planck)

The Magnetospheric Ion Composition Spectrometer (MICS) uses a conically shaped electrostatic analyser, a secondary-electron generation/detection system, and a solid state detector to measure the energy, TOF, and the energy per charge of the incident ion flux. These three parameters permit a unique determination of the ion charge state, mass, and incident energy over the energy range from $\sim$ 1.2 keV/Q to 426.5 keV/Q. MICS uses an unusual electrostatic filter design which combines a rather good definition of the incident particle direction (narrow acceptance angle) with high detection sensitivity (large acceptance area). The instrument's conceptually small angular cone in velocity space samples the pitch angle distribution of the energetic particle population with high angular resolution as the spacecraft rotates about its spin axis.

Low-Energy Magnetospheric Ion Composition Spectrometer

AFGL-701-11B
P.I.: E.G. Mullen (PLGD)
Co.-I.: T. Fritz (LANL)

The Low-Energy Magnetospheric Ion Composition Spectrometer (LOMICS) instrument is designed to distinguish and measure the velocity distributions of all important magnetospheric ion species up to 44 keV per charge. The sensor is mounted, together with HIT and their common data processing unit and power supplies, in the high-mass sensor-B unit. LOMICS consists of a conventional 90° spherical-section electrostatic analyzer (ESA) followed by a TOF analyser. The ESA provides ion energy/charge (E/Q) and angular analysis. The TOF analyser provides a time measurement that is proportional to ion velocity from which ion mass/charge (M/Q) can be determined.

The TOF mass analysis technique is usually restricted to high energy particles that undergo relatively little scattering and energy loss in generating start and stop signals. However, TOF analysis on low energy ($\sim$ eV) ions can be performed if energy/charge analysed ions are post-accelerated. At the lowest ion energies covered by LOMICS ($\sim$ 40 eV), a mass resloution of $M/\Delta M \sim 2$ can be achieved, which is sufficient for E/Q and M/Q analysis of the major magnetospheric ion species. Mass resolution should improve with increasing ion energy, which is one advantage of TOF over more conventional magnetic mass spectrometry in this energy range. A second

advantage, also exploited on LOMICS, is that large polar angles of acceptance are possible because of the compactness and low weight of the TOF design.

Heavy Ion Telescope

AFGL-701-11C
P.I.: E.G. Mullen (PLGD)
Co.-I.: T. Fritz (LANL)

The Heavy Ion Telescope (HIT) sensor uses a three-element solid state detector telescope to measure the rate of energy loss, the ion incident energy, and its time-of-flight (TOF). These three parameters permit a unique determination of the ion mass, elemental identification, and incident energy over the energy range from 100 keV per ion to 15000 keV per ion.

2.4.11 Spectrometer for Electrons and Protons

ONR-307-3
P.I.: R. Vondrak (LPARL)
Co.-I.: J. Quinn (LPARL)
R. Nightingale (LPARL)
H. Voss (LPARL)
R. Robertson (LPARL)

The Spectrometer for Electrons and Protons (SEP) measures with fine pitch angle resolution the flux of energetic electrons in the energy range of 20–5000 keV and the flux of energetic protons in the energy range 500 keV – 100 MeV. SEP consists of three identical particle telescopes composed of surface-barrier silicon detectors with active anticoincidence shielding and narrow collimation (3° FWHM). The energy spectra are measured with fine energy resolution: 24 contiguous channels for electrons, 48 contiguous channels for protons. The three particle telescopes are mounted at optimum angles to the CRRES spin axis to provide nearly complete pitch angle coverage on each spacecraft spin.

The overall objective of the SEP experiment is to obtain necessary data to construct predictive models, suitable for engineering purposes, of the energetic particle and plasma environment in those regions of space of primary interest to the DOD satellite operations.

2.4.12 Low Energy Ion Mass Spectrometer

ONR-307-8-1&2

P.I.: R. Vondrak (LPARL)
Co.-I.: J. Quinn (LPARL)
R. Nightingale (LPARL)
H. Voss (LPARL)
R. Robertson (LPARL)

The Low Energy Ion Mass Spectrometer (IMS-LO) is designed to measure plasmas that are sources of the radiation belt particles, and to provide data on the origin and acceleration processes of these plasmas. The instrument measures energy and mass spectra covering the ranges $E/Q = 0.11$–$35\,\mathrm{keV/e}$ and $M/Q = 1$–$32\,\mathrm{AMU/e}$ with good coverage of pitch angles throughout the orbit. These data will be used to investigate plasma interaction processes.

IMS-LO consists of two identical instruments which are mounted on the aft surface of the spacecraft whith their look directions at 135° and 105° to the spin axis. The look directions of the instruments were chosen to maximize coverage of fluxes near the magnetic field line direction throughout the mission.

The energy range of the instruments is covered by 45 energy steps, broken into three contiguous parts of 15 energy steps each. The three parts of the energy coverage are sampled in parallel by three separate analyser and sensor units (heads). At the completion of each 15-step sequence, the background counting rate is measured for each sensor head. The mass range is covered by 32 steps. Alternatively, the spectrometer can be commanded to a heavy-ion mode. In addition to ion measurements, each of the two instruments monitors the background electron flux at four fixed energies.

2.4.13 Medium Energy Ion Mass Spectrometer

ONR-307-8-3

P.I.: R. Vondrak (LPARL)
Co.-I.: J. Quinn (LPARL)
R. Nightingale (LPARL)
H. Voss (LPARL)
R. Robertson (LPARL)

The Medium Energy Ion Mass Spectrometer (IMS-HI) measures both the energetic ion composition and energetic neutral particle energy spectra and pitch angle distributions, with good mass, temporal, spatial, and energy resolution. IMS-HI extends the energy range of ion composition measurements well above that of the IMS-LO instruments.

The principle of IMS-HI is based on ion momentum separation in a magnetic field followed by energy and mass defect analysis using an array of cooled silicon solid state sensors. The instrument features a parallel architecture with simultaneous mass and energy analysis at relatively high sensitivity. IMS-HI is located at an angle of 75° to the spin axis to maximize pitch angle sampling. The ion energy range is approximately 20–8000 keV/AMU/Q.

2.4.14 Experiment for High Energy, Heavy Nuclei Composition

ONR-604

P.I.: J. Simpson (University of Chicago)
Co.-I.: M. Munoz (University of Chicago)
J. Wefel (Louisiana State University)

The overall scientific objectives of the Experiment for High Energy, Heavy Nuclei Composition are:

1. to obtain new data on the isotopic and elemental composition of high energy, heavy charged particles to assist in understanding the high energy conversion processes in solar flares;

2. to discover observable solar conditions leading to the explosive phase of a solar flare;

3. to determine the high energy, heavy ion fluxes in selected regions of the magnetosphere to determine its importance as a source of radiation damage and 'soft upsets' in electronic devices.

To achieve the high mass resolution needed for isotopic separation of heavy ions, the trajectory of each charged particle entering the acceptance cone of the telescope must be measured, both to correct the path length in the other detectors and to determine the arrival direction of the particles from space. A position-sensing detector (PSD) collects the charge liberated by the passage of the particle with a series of gold strips on its top surface. This signal is read out through a resistive divider network and compared with the total signal from the detector, obtained from the charge collected on the back surface contact, to obtain one coordinate of the point of incidence of the particle. Two sets of PSDs (three per set for redundancy) are used in the telescope to obtain the trajectory of the particle. Calibration of this system with accelerator particles shows that the position can be measured to < 0.1 mm, and the angle of incidence of the particle determined to $< 1°$.

A ground-commandable operations mode provides detailed analysis of proton and α particle flux levels. Thus, complete measurements can be obtained for any particle population observed. The instrument also measures protons and α particles over the energy range 25–119 MeV. In quiet regions of space, a priority system ensures that the heavy nuclei are analysed in preference to protons and α particles. In regions of high background radiation, a commandable heavy particle 'normal mode' is invoked. This mode suppresses the high firing rates induced by trapped protons and electrons while still permitting the rare heavy ions to be analysed. In normal mode, the instrument is practically insensitive to protons.

2.5 Plasma and Wave Experiments

The plasma and field sensors on CRRES were specifically designed to study the evolution of particle pitch angle distributions and to identify wave modes and free energy sources responsible for that diffusion.

The plasma and field instruments are a triaxial fluxgate magnetometer, a search coil magnetometer, a passive plasma sounder, and a Langmuir probe. The fluxgate magnetometer measures the local geomagnetic field. The particle detectors onboard use the magnetic field measurement for accurate determination of pitch angle. The local plasma sounder measures electrostatic and electromagnetic fluctuations over the frequency range 5.6 Hz to 400 kHz, and specifies plasma densities (n) in regions where $n < 2000\,\mathrm{cm}^{-3}$. Data from the Langmuir probe will be used to monitor the quasi-dc electric field. It is also programmable to measure either quasi-dc electric field or plasma densities in regions with $n > 1\,\mathrm{cm}^{-3}$. In addition, the Langmuir probe is able to access very small scale boundary features.

2.5.1 Fluxgate Magnetometer

AFGL-701-13-1
P.I.: E.G. Mullen (PLGD)
Co.-I.: H. Singer (PLGD)

The purpose of the Fluxgate Magnetometer Experiment is to measure the ambient geomagnetic field and low frequency variations in that field from dc to 8 Hz.

The Earth's magnetic field is measured by a triaxial fluxgate magnetometer at a rate of 16 times per second in the range ± 45000 nT. The three axes of the magnetometer are mutually orthogonal to approximately 0.08°. The sensors are mounted in a single housing on a rigid Astromast boom. The 6.1 m boom locates the sensors $\sim$ 7.5 m from the centre of the spacecraft to fulfill the requirement of

having less than a few nT of vehicle-generated magnetic field at the sensor location. The analog electronics to operate the sensors are mounted inside the spacecraft and connected to the Electric Field/Langmuir Probe (EF/LP) experiment for power, signal processing and telemetry formatting.

The signal from each sensor is sent to the Langmuir Probe electronics where it is filtered with a 6 Hz lowpass cutoff to prevent aliasing from signals above the 8 Hz Nyquist frequency, and sampled by a 12-bit A/D convertor in the ranges ± 45000 nT and ± 850 nT to provide low and high sensitivity, respectively. For each sample from each axis, a microprocessor determines whether to enter the high or low sensitivity value into the telemetry stream. Furthermore, once per second the field strength at low sensitivity from all axes will be included in the data stream. The magnetometer data can also be sampled in a burst mode as described in the EF/LP instrument section. Additionally, the fluxgate signal will be lowpass filtered with a 20 Hz cutoff and provided to the spacecraft in analog form in two different ranges, ± 45000 nT and ± 1000 nT.

The magnetometer provides a real time signal to LEPA to enable this instrument to determine which zone in the field of view of its detectors is observing nearly along the magnetic field direction. LEPA is then able to transmit high time-resolution data, a complete energy spectrum in 0.5 s, with about 1° pitch angle resolution from the zone that is making observations near or within the particle loss cone.

On command, the signal from the near spin axis, the Y magnetometer sensor, can be amplified six times, in either the high-gain or low-gain mode, to provide better amplitude resolution at low field strengths near apogee. The increased sensitivity facilitates the detection of high-frequency, low-amplitude waves, such as ion-cyclotron waves that interact strongly with the plasma environment.

2.5.2 Passive Plasma Sounder and Search Coil Magnetometer

AFGL-701-15/AFGL-701-13-2

P.I.: E.G. Mullen (PLGD)
Co.-I.: R. Anderson (University of Iowa)
D. Gurnett (University of Iowa)
H. Singer (PLGD)

The purpose of the Passive Plasma Sounder and Search Coil Magnetometer Experiments, collectively known as the SPACERAD Plasma Wave Experiment, is to measure the plasma wave environment in the Earth's radiation belts. Emphasis is on high frequency and time resolution, high sensitivities (low noise levels), a large dynamic range, and sufficient frequency response to cover all the characteristic fre-

quencies of the plasma that are of interest. The experiment provides measurements of electric fields from 5.6 Hz to 400 kHz with a dynamic range of at least 100 dB (a factor of 10^5 in amplitude) beginning at the respective receiver's noise level. Magnetic field measurements from 10 to 400 kHz are also possible but the dynamic range will be reduced due to the roll-off of the search coil magnetometer above 10 kHz. These ranges adequately cover the expected range of plasma wave amplitudes detected by the electric and magnetic sensors.

The 5.6 Hz to 400 kHz frequency range of the Plasma Wave Instrument covers most of the important characteristic frequencies that CRRES encounters in the region above about $2\,R_E$. Below about $2\,R_E$, when the plasma frequency exceeds 400 kHz, the Electric Field/Langmuir Probe Experiment provides the electron number density measurements. Electromagnetic plasma waves below 5.6 Hz are in the frequency range covered by the Fluxgate Magnetometer. Electric field fluctuations below 5.6 Hz are measured by the Langmuir Probe. The SPACERAD Plasma Wave Experiment instrumentation will not only measure and characterize the plasma wave environment, but will also measure the electron number density and help identify the region of space the satellite is in.

The Plasma Wave Experiment measures the electromagnetic and/or electrostatic fields detected by three sensors:

1. a 100 m tip-to-tip extendable fine wire long electric dipole antenna,
2. a search coil magnetometer mounted at the end of a 6 m boom,
3. a 94 m tip-to-tip spherical double probe electric antenna.

The first two sensors are the primary sensors for the Plasma Wave Experiment, the third sensor is the primary sensor for the Electric Field/Langmuir Probe Experiment.

2.5.3 Electric Field/Langmuir Probe Instrument

AFGL-701-14

P.I.: E.G. Mullen (PLGD)
Co.-I.: F. Mozer (University of California Berkeley)
J. Wygant (University of California Berkeley)
N. Maynard (PLGD)
M. Smiddy (PLGD)
H. Singer (PLGD)

The Electric Field/Langmuir Probe (EF/LP) experiment is designed to measure variations in cold electron temperature and density and in electric fields, which are crucial to the understanding of the wave modes and instabilities responsible for

wave-particle interactions. In addition, the ability of the instrument to measure quasistatic dc electric fields at and within geosynchronous orbit allows a detailed study of electric fields responsible for the earthward convection of particles from the plasma sheet, and the radial diffusion and energization of radiation belt particles to energies up to 1 MeV.

The EF/LP instruments consist of a main electronics package on the spacecraft body and two pairs of orthogonal sensors with tip-to-tip separations of about 100 m in the spin plane of the satellite. At the tips of opposing booms are conducting sensors. For one set of booms, these sensors are spheres. For the other, they are cylindrical antennas shared by the Passive Plasma Sounder and the EF/LP. The instrument provides measurements of the quasistatic two-dimensional electric field in the spin plane of the spacecraft at a rate of 32 samples/s, a sensitivity of better than 0.1 mV/m, and a dynamic range of 1000 mV/m. The spherical probes can be periodically swept in either current or voltage to determine plasma density and temperature through ground analysis of the resulting Langmuir characteristic curve. The measurement is accurate for densities between 0.1 and 10^4 electrons/cm^3 and electron temperatures ranging from a fraction of an eV to 100 eV. The instrument also has a programmable burst memory which can provide selected high-time resolution data at cumulative rates up to 50000 samples/s.

The Langmuir Probe has two different operating modes which are controlled by an on-board microprocessor. In the electric field mode, the sensors are current-biased and measure electric fields by determining the potential difference between opposing sensors. When the instrument is operated in the Langmuir probe mode, the spherical sensors are biased at fixed and stepped potentials relative to the plasma, and the current collected by the spheres is measured. The resulting Langmuir curve provides information on cold electron temperature and density.

The EF/LP instrument provides electric field measurements in an analog form to LEPA for onboard correlation with particle measurements, and also shares the electric field booms with the passive plasma sounder.

Chapter 3

Data availability and quality

The final calibrations of the raw data from the CRRES instruments in terms of physical quantitities is still under way for most experiments. In the mean time, preliminary data sets have been made available.

The first data set to be issued was the Science Summary Data Base (SSDB). This data base provides the user with one-minute averages of the data from selected instrument channels, which have been converted very tentatively to physical quantities. Several versions of ephemeris data were also issued. The most recent version was generated on an orbit-by-orbit basis and gives the orbital elements at one minute and five minute intervals for low and high altitudes, respectively.

The data from the Space Radiation Dosimeter have by now been fully calibrated (Gussenhoven & Sperry 1992) and are available at PLGD. For the other instruments of interest to the TREND-2 project, the final data sets are foreseen for the first half of 1993. However, in order to enable users to familiarize themselves with the data, a limited set of provisionally calibrated PROTEL and HEEF data have been made available.

In the following sections, we describe the format of the SSDB and of the Time History Data Bases (THDBs) for the CRRES instruments relevant to the TREND-2 project. We also present results obtained from an analysis of the SSDB, which is useful to get a general impression of the possibilities and limitations of the CRRES data sets.

3.1 The Science Summary Data Base

The CRRES Science Summary Data Base (SSDB) contains preliminary data of several CRRES detectors. It was released to provide the community with a quick survey of the available data, for instance to identify a period of interest in the CRRES

mission for a later in-depth analysis. There has been no attempt to apply any quality control criteria to the data (removal of noise spikes etc.). Only preliminary calibration factors have been applied, and many instruments require background subtraction. However, even with these limitations, it is possible to draw some general conclusions and results from the SSDB (cf. Sect. 3.1.3 and 3.1.4).

3.1.1 Data format

The SSDB files were distributed in ASCII format. In order to obtain a more compressed format and to improve access speeds, the original files were transformed into Fortran unformatted files. At the same time, information from the ephemeris files was added, so that only one file needs to be accessed for a given orbit. The resulting SSDB files are organized on an orbit by orbit basis. They are named SSDB_EPHXXXX, where XXXX is the orbit number, left filled with zeroes. Each file contains a header record and approximately 600 data records with 21 entries per record. The contents of the header and data records are listed in Table 7.

Fluxes in Table 7 are given in units of particles/ (cm^2 s sr MeV), count rates are in counts/s. The special value -1×10^{30} is the value written for data items when dropouts occurred. For MEES, negative values for the difference between average counts and background counts are indicated by the special value -0.5×10^{30}. The model magnetic field strengths and L-values were obtained with a combination of the IGRF 90 model and the Olson-Pfitzer (1977) quiet model.

3.1.2 Implementation of ephemeris data

A first study of the SSDB for ESTEC was made by Heck (1992). At the time this study was made, the available ephemeris data were given at 10 minute intervals. This meant that the ephemeris had to be interpolated for the times in the SSDB. Heck performed this interpolation by fitting a spline to the four ephemeris points closest to the times in the SSDB.

When more accurate ephemerids became available, with a resolution of 1 minute below 3 R_E and of 5 minutes at higher altitudes, we produced a new version of the SSDB_EPHXXXX files described in Sect. 3.1.1, by interpolating with a parabolic curve through the three ephemeris points closest to the SSDB times. The resulting interpolated ephemeris is very close to Heck's version at altitudes above a few thousand kilometers. However, at lower altitudes, there are significant differences. On average, the altitudes around perigee in our ephemeris are about 60 km lower than the altitudes in Heck's ephemeris. This difference in illustrated in Fig. 3, representing the altitude for orbit 250 in function of time up to 1500 km, for both versions of the interpolated ephemeris. The result of this difference is further illustrated in Fig.

Table 7. Record structure of the SSDB header and data records. All entries are 4 byte REAL, except when otherwise indicated.

Entry	Description
	Header Record (INT*2)
1	Year
2	Day of year
3	Orbit number
4	Time resolution (60 seconds)
	Data Records
1	UT (seconds)
2	L (R_E)
3	Solar magnetic latitude (degrees)
4	Solar magnetic local time (hours)
5	Measured magnetic field magnitude (nT)
6	Model magnetic field magnitude (nT)
7	$(B_{measured} - B_{model})/B_{model}$
8	Electron flux, 4–5 MeV (HEEF L6-L7)
9	Electron countrate, > 2.5 MeV (Space Radiation Dosimeter LOLET 2)
10	Electron flux, 1–1.5 MeV (HEEF LL-L1)
11	Electron flux, 0.2–0.3 MeV (MEES channel 2)
12	Electron flux, 20–385 keV (EPAS 90° look direction)
13	He countrate, > 45 MeV/Nucleon (Experiment for High Energy Heavy Nuclei Composition P2)
14	Star countrate, > 75 MeV (Space Radiation Dosimeter VHILET 4)
15	Proton countrate, > 35 MeV (Space Radiation Dosimeter HILET 2)
16	Proton flux, 44.3–53.5 MeV (PROTEL HEH 13)
17	Proton flux, 3.1–4.1 MeV (PROTEL LEH 5)
18	Electron flux, 558–649 keV (MEES channel 6)
19	Geodetic altitude (km)
20	Western longitude (degrees) multiplied by 10 (INT*2)
21	Geodetic latitude (degrees) multiplied by 10 (INT*2)

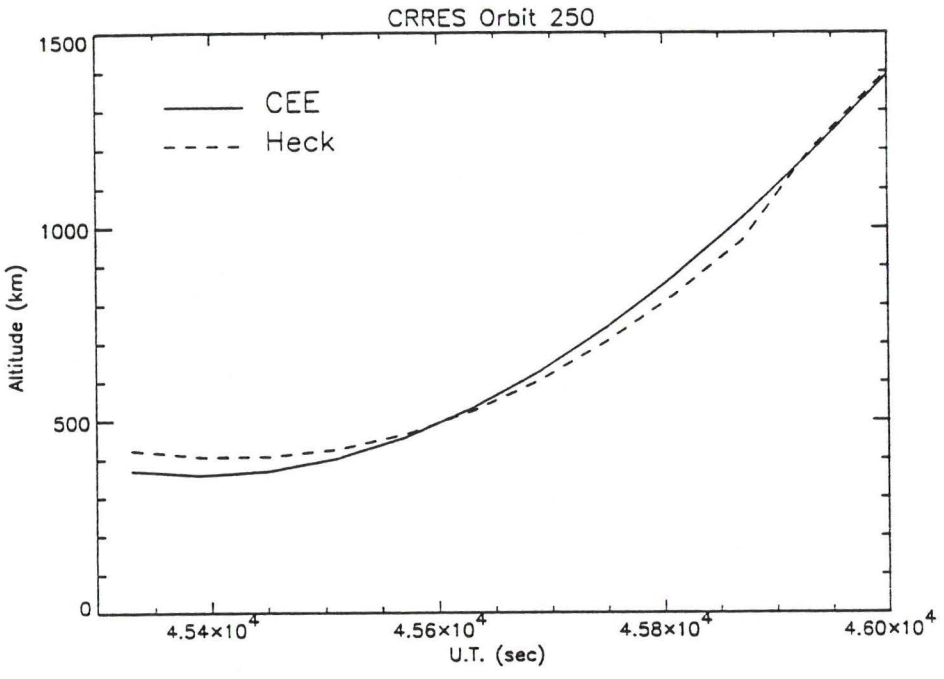

Figure 3. CRRES altitudes for orbit 250 up to 1500 km derived from Heck's (dashed line) and our (solid line) version of the interpolated ephemeris.

4, where we plot the perigee altitude obtained with both versions of the ephemeris. The altitudes obtained by Heck oscillate on a short time scale with an amplitude of about 60 km, while for our altitudes the amplitude is only a few kilometers. The oscillation in Heck's data is caused by the spline interpolation at low altitudes. When a more physical interpolation, based on methods of celestial mechanics, is used, the resulting perigee altitudes closely follow the solid line in Fig. 4. The situation for the perigee latitudes, represented in Fig. 5, is similar.

We also found that not all SSDB files contain data for a complete orbit. For about 30 orbits, the first SSDB data point does not correspond to the first point in the ephemeris. Consequently, the correct ephemeris points for interpolation have to be located first, which was not taken into account by Heck. As a result, Heck's orbits are shifted with respect to the true orbit. We illustrate this in Fig. 6, where altitude is plotted in function of time for orbit 451. It can be seen that the shift in orbit leads to differences in altitude of the order of 1000 km. Finally, three SSDB files only contain data around apogee. However, Heck's interpolation procedure fitted these points with the first points in the corresponding ephemeris files, i.e. the perigee of the orbit. Naturally, this results in a completely discordant interpolation.

The influence of these incorrectly interpolated orbits is considerable, as will be discussed in the following sections on the analysis of the SSDB data. It is already apparent in Fig. 5: the few scattered points are due to the anomaly described in

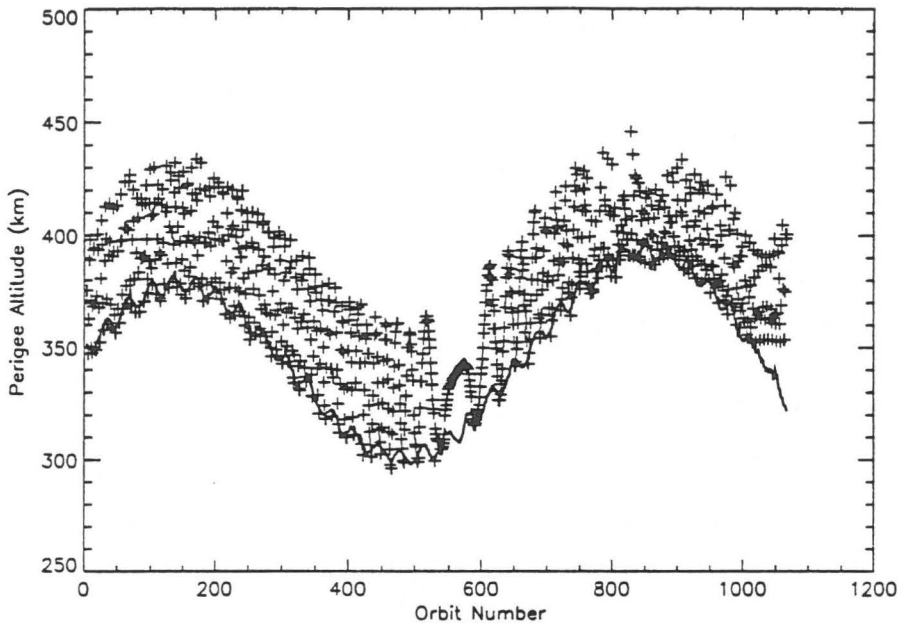

Figure 4. Comparison of CRRES perigee altitudes derived from Heck's (crosses) and our (solid line) version of the interpolated ephemeris.

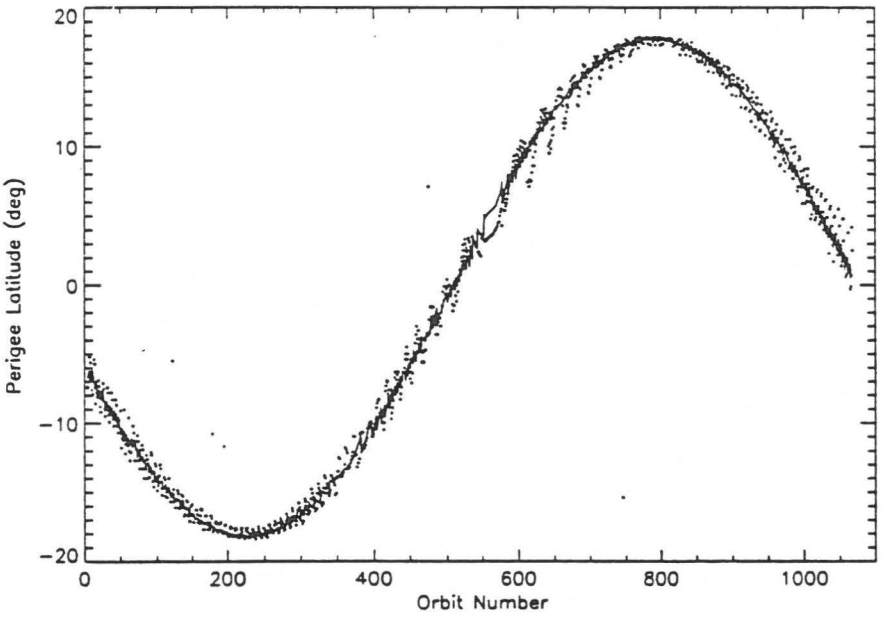

Figure 5. Comparison of CRRES perigee latitudes derived from Heck's (dots) and our (solid line) version of the interpolated ephemeris.

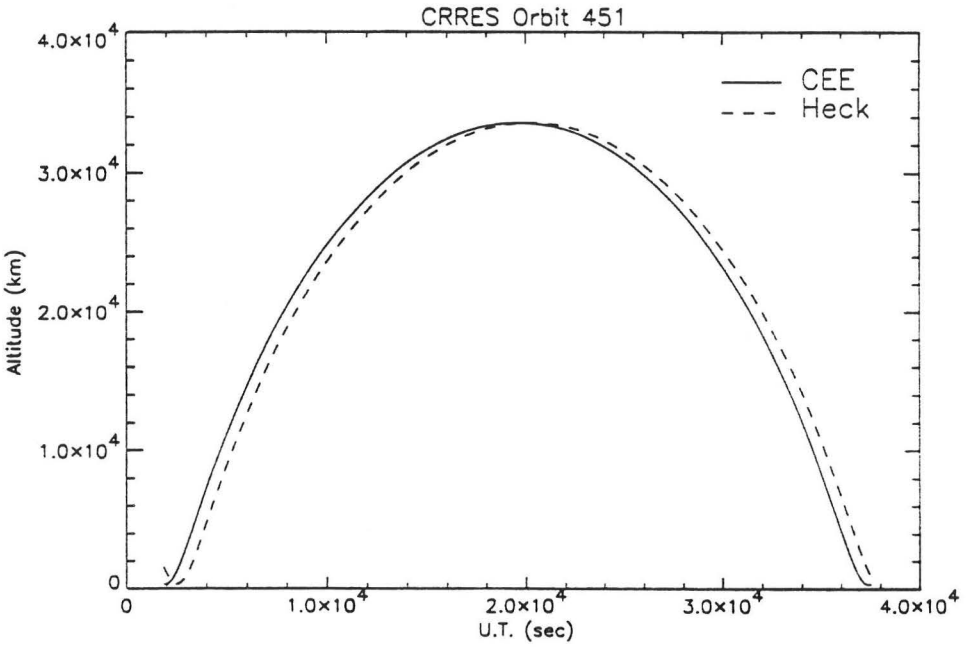

Figure 6. CRRES altitude for orbit 451 in function of time, for Heck's (dashed line) and our (solid line) version of the ephemeris.

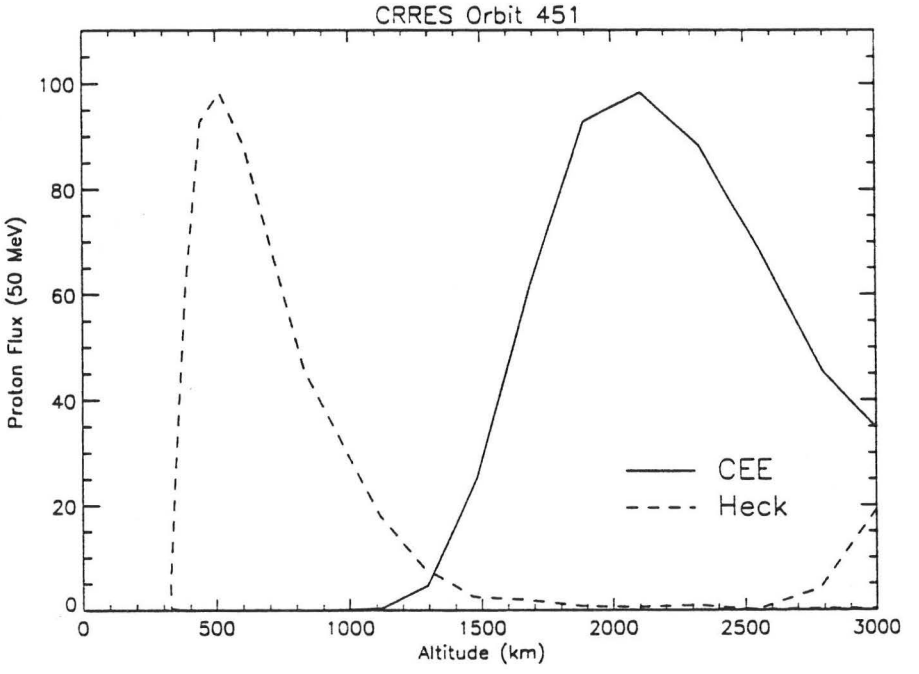

Figure 7. SSDB differential proton flux at 44.3–53.5 MeV for orbit 451, in function of altitude, for Heck's (dashed line) and our (solid line) version of the ephemeris.

this section. The corresponding points in Fig. 4 are off the scale of the graph. The effect of the incorrect interpolation on the flux distribution can be seen in Fig. 7, where the differential proton flux at 44.3–53.5 MeV is plotted in function of altitude for orbit 451, for both versions of the ephemeris. Heck's ephemeris predicts a large flux at around 500 km, while in reality this maximum lies much higher, i.e. around 2000 km.

3.1.3 Comparison with NASA radiation belt models

Heck (1992) compared the CRRES proton and electron fluxes in the SSDB with the NASA radiation belt models AP-8 MAX and AE-8 MAX. It appeared that even with the SSDB data, clear discrepancies with the NASA models can be identified.

It was found that the electron fluxes predicted by the NASA model are on the average much higher than the fluxes in the SSDB. In particular, the inner zone fluxes predicted by the model are orders of magnitude higher than the CRRES fluxes, due to the very low proton contamination of the CRRES electron fluxmeters. Also, the time dependence of the outer zone electron population is very clear in the SSDB data and naturally absent in the NASA model.

The differences between model and SSDB fluxes are smaller for protons. Although the model fluences are generally too high, the orbit averaged fluences do not differ too much. However, the NASA model naturally fails to predict the emergence of a secondary proton belt following the March 1991 SSC.

3.1.4 Location of the South Atlantic Anomaly

Heck (1992) used the CRRES SSDB to locate the South Atlantic Anomaly (SAA). In Fig. 8, the differential proton flux above $15\,(\mathrm{cm}^2\,\mathrm{s\,sr\,MeV})^{-1}$ at 44.3–53.5 MeV, averaged over orbits 4–463 for altitudes below 1000 km, is shown in function of longitude and latitude. The SAA is not as clearly defined as expected, and high fluxes are seen at unexpected locations.

Most of the spread on the SAA fluxes in Fig. 8 is artificial and caused by the interpolation errors for incomplete orbits that we discussed above. The same plot, but now with our version of the ephemeris, is represented in Fig. 9. It is seen that the highest fluxes are now constrained to the expected location of the upper part of the SAA. When the deviant orbits are eliminated from Fig. 8, the difference with Fig. 9 becomes very small.

An alternative method to define the location of the SAA consists of averaging particle fluxes or dose counts over longitude intervals of a given width, and plotting the resulting averages in function of longitude. Heck's (1992) plots of these averages only give a very crude approximation to the location of the SAA, with local maxima

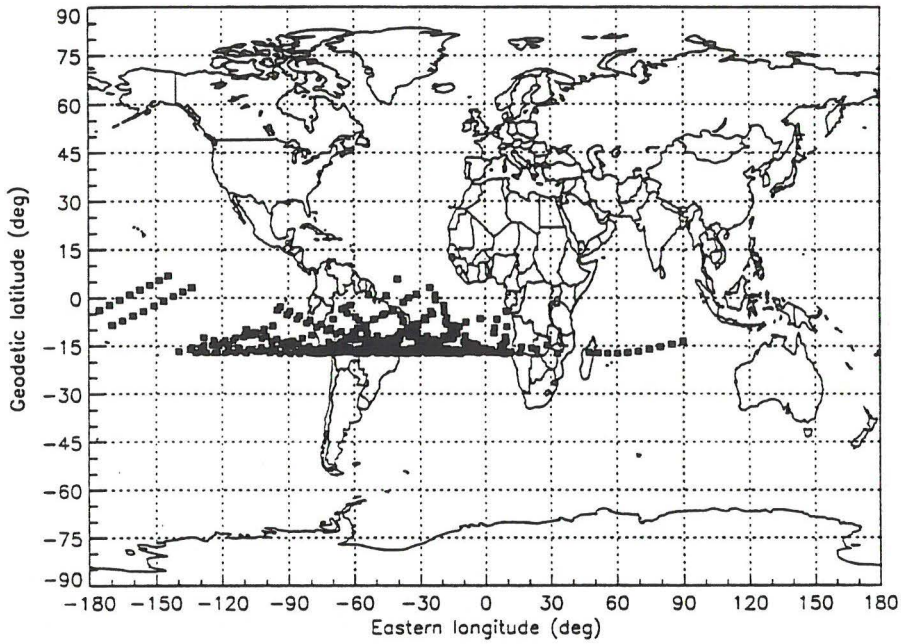

Figure 8. SSDB differential proton flux at 44.3–53.5 MeV, above 15 $(\mathrm{cm}^2\,\mathrm{s\,sr\,MeV})^{-1}$, averaged over orbits 4–463 for altitudes below 1000 km, in function of longitude and latitude (Heck's ephemeris).

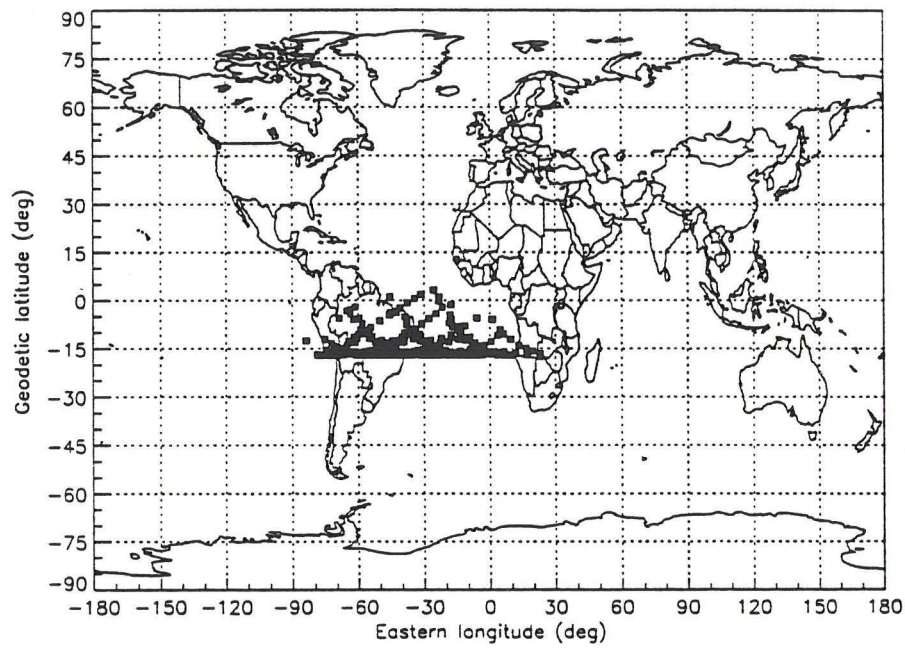

Figure 9. SSDB differential proton flux at 44.3–53.5 MeV, above 15 $(\mathrm{cm}^2\,\mathrm{s\,sr\,MeV})^{-1}$, averaged over orbits 4–463 for altitudes below 1000 km, in function of longitude and latitude (our ephemeris).

appearing at other longitudes as well. We repeated this procedure with the new ephemeris. The results are shown in Fig. 10. For most of the particle data, the SAA is now clearly defined in longitude, and no other maxima appear. Again, when the discordant orbits are removed from Heck's averages, the result is almost identical to Fig. 10.

3.2 The Time History Data Bases

The data bases of the CRRES experiments are organized in a modular data management system. Initial agency tape files were created with separate ephemeris, attitude, and magnetic field files. From these files, the Time History Data Base (THDB) is constructed. It is a data base ordered by time and instrument, in which the raw data are kept at the highest time resolution of the instrument along with calibration and comment files which contain information on how to convert raw telemetry counts into engineering units. THDB files are produced on an instrument by instrument and orbit by orbit basis. An orbit is defined as a spacecraft revolution starting at perigee and ending at the following perigee.

The THDB for the CRRES mission has been designed and implemented by the Institute for Space Research at Boston College. The THDB consists of structured, time ordered files of spacecraft sensor data, calibration files, attitude fit coefficient files, and ephemeris files.

The THDB files, except for the calibration and attitude fit coefficient files, are generated in integer form (allowing ready access from various computer systems) and consist of time tagged structured data. All parameters are stored in INT*4, INT*2 or INT*1 form.

THDB files containing sensor data consist of a header record followed by a series of data records. Each file is of fixed record structure. In general, the sensor data is stored at the full data rate. Data records consist of a UT time tag and data grouped into logical structures.

For some sensors, the algorithms necessary to convert the telemetry data to science units are extremely complex. For these sensors, pre-processed files are generated which are used as input to analysis routines which produce the science unit output. These files do not strictly fit the concept of the THDB, but are nevertheless referred to as THDB structures.

Validation of the data in the THDB is a major task. Shortly after CRRES was launched, all software used to create the THDB from agency tapes was verified. Before the data can be used for analysis, ongoing quality checks must be performed to remove spurious noise, contamination from unwanted particles, temperature effects, etc. . Also, calibrations have to be verified with on-orbit data, and cross-calibrations

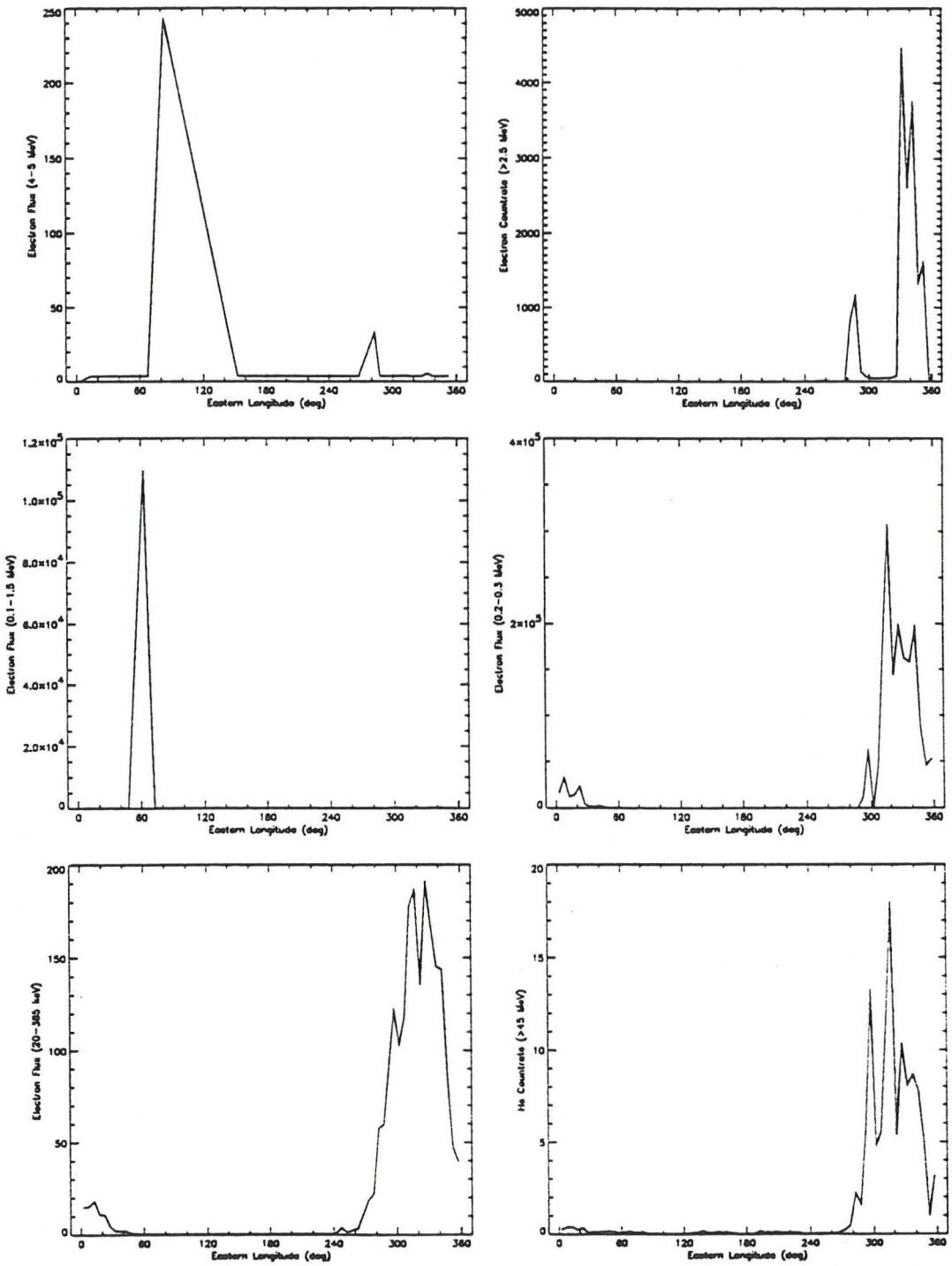

Figure 10. SSDB particle fluxes and count rates, averaged over 5° longitude intervals, for orbits 4–463, in function of longitude (our ephemeris).

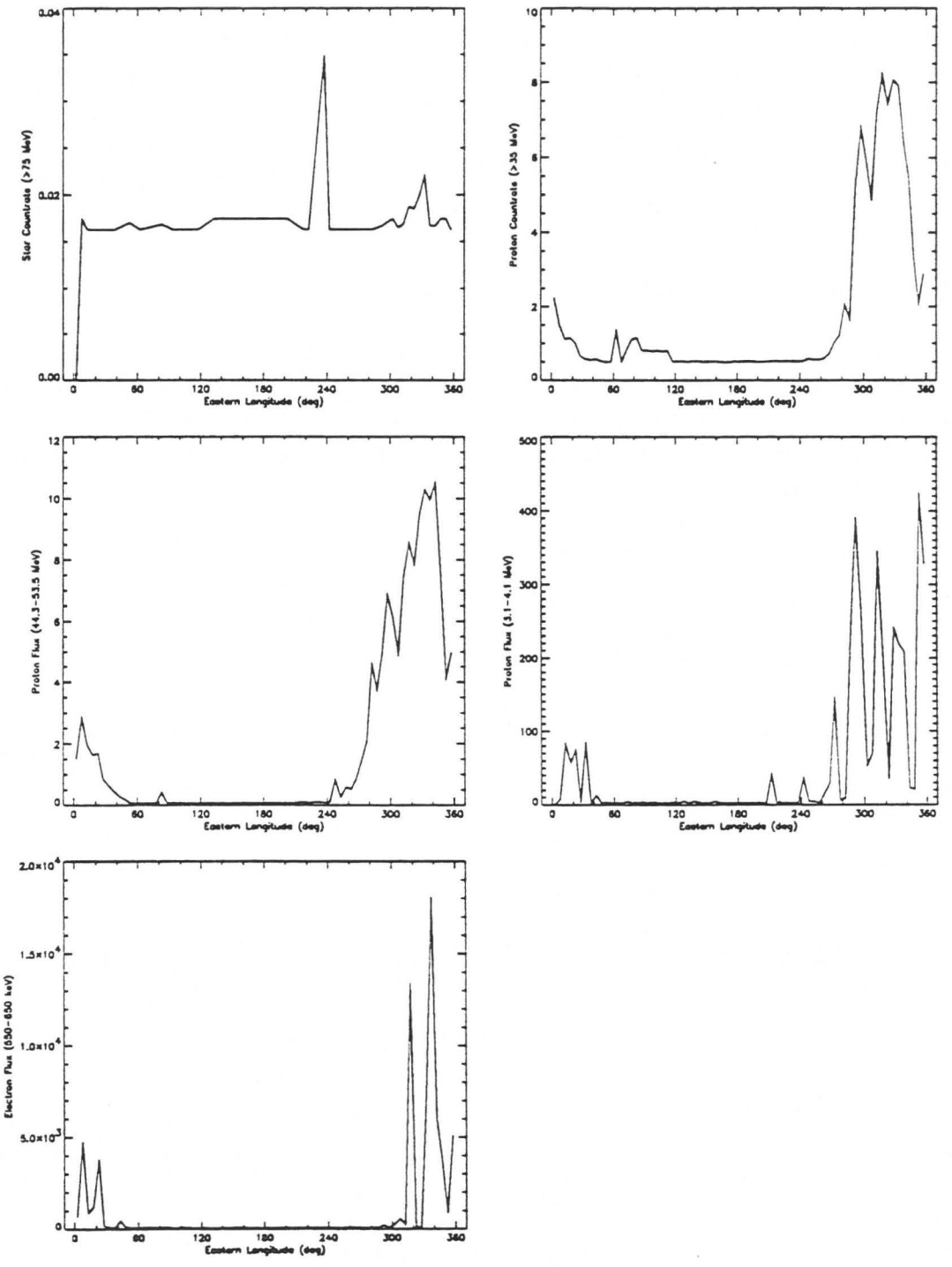

Figure 10. (Continued)

of instruments which overlap in energy are necessary.

A complete description of the THDB files for all instruments has been compiled by Delorey (1991). The generation of the CRRES agency tapes has been documented by Griffin et al. (1989). In the following sections, we summarize the structure of the THDB files for the experiments of direct interest to TREND-2, i.e. Space Radiation Dosimeter, HEEF, MEES, EPAS, PROTEL, SEP, Fluxgate Magnetometer, and ephemeris and attitude determination data.

3.2.1 Space Radiation Dosimeter

The THDB for this sensor is a pre-processed file consisting of compressed counts for all readouts. This pre-processed file has been transformed into orbit files (P002 files) by E. Holeman of PLGD. The orbit files contain the universal time of each 4.096 second observation and the following dosimeter data for HILET and LOLET, domes 1, 2, 3, 4:

1. running sum of dose counts,
2. dose counts per 4.096 s observation,
3. star counts per 4.096 s observation,
4. flux counts per 4.096 s observation.

Negative dose counts were inserted in the P002 files when the dose counts for a 4.096 s observation could not be correctly determined.

The background correction for the flux and the conversion of dose counts to dose are calculated in the following way:

1. Dose counts (DC) are converted to Dose Counts per Second (DCS) as

$$\mathrm{DCS} = \frac{\mathrm{DC}}{\mathrm{NOB} \times 4.096\,\mathrm{s}}$$

   where NOB represents the number of observations.

2. DCS is converted to average dose (DOSE) using calibrations factors (CALFACs) based on calibration data from the instrument:

$$\mathrm{DOSE} = \mathrm{DSC} \times \mathrm{CALFAC}\,.$$

   The average dose is expressed in Rads/s.

Table 8. Calibration factors for the Space Radiation Dosimeter.

	Dome 1	Dome 2	Dome 3	Dome 4
		DCS to DOSE (CALFAC)		
HILET	3.24×10^{-3}	1.93×10^{-3}	1.84×10^{-3}	8.3×10^{-4}
LOLET	1.18×10^{-2}	1.85×10^{-3}	1.86×10^{-3}	2.0×10^{-4}
		α Source Dose (ALPHAD)		
HILET	1.750×10^{-4}	4.480×10^{-6}	8.900×10^{-6}	9.220×10^{-7}
LOLET	5.782×10^{-6}	7.770×10^{-7}	9.114×10^{-7}	9.800×10^{-8}
		α Source Flux Counts per Second (ALPHAF)		
HILET	2.45	0.49	0.79	0.196
LOLET	0.42	0.056	0.052	0.116

3. The background dose from the α source (ALPHAD) is then subtracted from the average dose, resulting in the Corrected Dose (CD), in units of Rads/s:

$$\mathrm{CD} = \mathrm{DOSE} - \mathrm{ALPHAD}\,.$$

4. The flux counts are converted to Flux Counts per Second (FCS):

$$\mathrm{FCS} = \frac{\text{Sum of Flux Counts}}{\mathrm{NOB} \times 4.096\,\mathrm{s}}\,.$$

5. The Corrected Flux Count per Second (CFCS) is obtained by subtracting the background due to the α source (ALPHAF) from the Flux Counts per Second:

$$\mathrm{CFCS} = \mathrm{FCS} - \mathrm{ALPHAF}\,.$$

The HILET and LOLET calibration factors are listed in Table 8 for dome 1, 2, 3, 4, respectively.

3.2.2 High Energy Electron Fluxmeter

The THDB has the compressed counts from 12 integral flux and singles channels, the 10 differential flux channels (LL, L1, L2, ..., L9) in the range 1–10 MeV, and a packed word consisting of three discretes and the PCM counts for the HV monitor. For the differential flux data, decompression of the counts is not required. The

differential flux, integral flux, and singles data are stored in 16 bit words. One THDB record is generated for every 4 minor telemetry frames.

The decompression algorithm for the integral flux and singles channels is

$$\text{TRUE COUNTS} = \text{M} \times 2^{\text{E}},$$

where M is the mantissa and E is the exponent. Conversion of decompressed counts to both integral flux and differential flux is performed by means of one multiplicative constant per channel. The data word length for the singles channels and integral flux values varies from 11 to 13 bits.

The time tag associated with each THDB record is the time at which the data was placed in the telemetry stream. The data was accumulated during the previous 4 minor frame intervals (nominally 512 ms). Data for this sensor is acquired for all spacecraft telemetry modes.

Table 9. Record structure of the HEEF header and data records.

Word	Description
	Header Record
1	Experiment ID (7014)
2	Year
3	Day of year
4	Orbit number
5	Start time of orbit (UT in milliseconds)
6	End time of orbit (UT in milliseconds)
7–16	Vacant (zero fill)
	Data Records
1	UT (milliseconds)
2–6	Compressed counts for the 10 point differential electron spectrum. The word order is L9, L8, ..., L1, LL.
7–12	Compressed counts for the singles channels and the integral channel. The word order is S2F, S1F, W1F, W2F, S2B, S1B, W1B, W2B, L10S, L10C, BGO, LS.
13	Bilevels MB1, MB2, MB3 and 8 bit HVM counts stored in the 11 LSBs.
14	Dropout flag
15–16	Vacant

The THDB file consists of a 16 word (32 bit words) header record followed by a series of data records. There is one data record per 0.512 s (4 TLM frames). The compressed counts for the differential and integral channels as well as the singles channels are stored in 16 bit words. Table 9 gives the record structure of the header and data records. The dropout flag has the value 1 if dropout occurred anywhere withing the 0.512 s period. Dummy fill (1's fill) is used for dropout within a spectrum.

The calibration file consists of ASCII data. The file contains a series of header records, comment records, energy value records associated with the differential channels, geometric factor records for the differential channels, and channel dependent constant records for the computation of the integral flux. There is one information word per record.

3.2.3 Medium Energy Electron Spectrometer

The THDB records contain compressed counts representing differential flux from 17 electron channels (0.1–1.7 MeV) every 0.512 s. The time tag on the THDB records is the time at the start of the minor frame on which the data was placed in the telemetry stream. The spectrum data was accumulated during the previous 0.512 seconds.

The decompression algorithm to convert compressed counts to true counts requires the extraction of the 3 MSBs and the 9 LSBs from the 12 bit word, representing the exponent (E) and the mantissa (M), respectively. The compressed counts are converted to true counts as

$$\begin{aligned} \text{COUNTS} &= \text{M} && \text{if E} = 0\,, \\ \text{COUNTS} &= 2^{(\text{E}-1)} \times (512 + \text{M}) && \text{if } 0 < \text{E} < 8\,. \end{aligned}$$

Conversion of the decompressed counts into differential number flux is accomplished as

$$\text{FLUX(i)} = \frac{\text{COUNTS(i)} - \text{COUNTS(16)} \times \text{K(i)}}{\text{GEF(i)} \times 0.512} \qquad \text{i} = 0, \ldots, 17\,,$$

where COUNTS(16) represents background counts and COUNTS(i) the counts for channel i, K(i) are channel dependent constants (~ 1), and GEF(i) are the combined geometric and efficiency factors used to convert to flux.

The THDB files for this sensor consist of a header record (in 32 bit integer form) followed by a series of data records. The THDB data records contain medium energy electron data for 17 differential electron energy channels plus one background channel, stored in 16 bit words (two 16 bit words per 32 bit word). The vacant flag word at the end of each record has the value 0 for normal operations or 1 to indicate that a data gap occurred due to the spacecraft telemetry mode being changed to

Table 10. HEEF Calibration file record structure.

Record	Description
	Header Records
1	Number of calibration files
2	Number of header records that follow (9) (I)
3	Experiment number (AFGL 7014) (CHAR*20)
4	Calibration version number (I)
5	Valid start date for calibration (e.g. 89105) (I)
6	Valid end date for calibration (I)
7	Number of record types in calibration file (4) (I)
8	Number of comment records (I)
9	Number of energy channel records (I)
10	Number of geometric factor records for differential flux (I)
11	Number of channel constant records for integral flux (I)
	Comment Records
1–N	Comment records (CHAR*80)
	Energy Channel Records (REAL)
1	L9
2	L8
⋮	⋮
9	L1
10	LL
	Geometric Factor Records (REAL)
1	GF for L9
2	GF for L8
⋮	⋮
9	GF for L1
10	GF for LL
	Channel Dependent Constant Records for Flux (REAL)
1	Constant for S2F (background)
2	Constant for SF1
⋮	⋮
10	Constant for L10C
11	BGO
12	LS

Table 11. Record structure of the MEES header and data records.

Word	Description
	Header Record
1	Experiment ID (70151)
2	Year
3	Day of year
4	Orbit number
5	Start time of orbit (UT in milliseconds)
6	End time of orbit (UT in milliseconds)
7–12	Vacant (zero fill)
	Data Records
1	UT (milliseconds)
2	Compressed counts for E0 and E1
3	Compressed counts for E2 and E3
4	Compressed counts for E4 and E5
5	Compressed counts for E6 and E7
6	Compressed counts for E8 and E9
7	Compressed counts for E10 and E11
8	Compressed counts for E12 and E13
9	Compressed counts for E14 and E15
10	Compressed counts for E16 (background) and E17
11	Byte 3: Vacant Byte 2: Telemetry dropout flag (normal value is 0, value is 1 if dropout in this frame) Byte 1: Bit 7: Sync indicator (0: sync ok, 1: sync mismatch) Bit 6: C (calibration flag) Bit 5: K (RAM check status) Bit 4: N (format mode) Bit 3: S (Sun pulse bit) Bit 2: T (contents of TM) Bit 1: W (RAM reload) Bit 0: Telemetry flag; normally 0, set to 1 if a data gap follows due to a switch to CSM or LASSII telemetry mode.
12	Vacant

Table 12. MEES Calibration file record structure.

Record	Description
	Header Records
1	Number of calibration files
2	Number of header records that follow (9) (I)
3	Experiment number (AFGL 7015A) (CHAR*20)
4	Calibration version number (I)
5	Valid start date for calibration (e.g. 89105) (I)
6	Valid end date for calibration (I)
7	Number of record types in calibration file (4) (I)
8	Number of comment records (I)
9	Number of energy channel records (I)
10	Number of geometric/efficiency factor records (I)
11	Number of channel constant records (I)
	Comment Records
1–N	Comment records (CHAR*80)
	Energy Channel Records (REAL)
1	E0
2	E1
⋮	⋮
16	E15
17	E16 (background)
18	E17
	Geometric/Efficiency Factor Records (REAL)
1	GEF0
2	GEF1
⋮	⋮
16	GEF15
17	GEF16 (background)
18	GEF17
	Channel Dependent Constant Records (REAL)
1	K0
2	K1
⋮	⋮
16	K15
17	K16 (background)
18	K17

CSM or LASSII mode. Each record has data accumulated over 4 telemetry frames (0.512 s). Dropout words within a spectrum are noted by 1's fill. If dropout occurs over a full spectrum, there is no fill: the data is simply missing. The header and data record structures are listed in Table 11.

The calibration file consists of ASCII data. The file contains a series of header records, comment records, energy value records, geometric factor records, and channel dependent constant records. There is one information word per record. The record structure of the calibration file is given in Table 12.

3.2.4 Electron Proton Angle Spectrometer

The THDB for EPAS has one record per four minor telemetry frames (0.512 s) and contains the compressed counts (in byte form) from

1. the two 14 point electron spectra (20–250 keV) and the associated detector numbers;
2. the 12 point proton spectrum (30 keV – 20 MeV) and the associated detector number;
3. the 10 electron and 4 proton integral flux values;
4. the proton coincidence and background counting rates;
5. selected discretes.

For the 8 bit compressed counts values, the 4 MSBs of the word represent the exponent (E) and the 4 LSBs represent the mantissa (M). The decompression algorithm is

$$\begin{aligned} \text{COUNTS} &= \text{M} && \text{if } \text{E} = 0\,, \\ \text{COUNTS} &= 2^{(\text{E}-1)} \times (16 + \text{M}) && \text{if } 0 < \text{E} < 16\,. \end{aligned}$$

A data record is written once every 0.512 seconds.

Each record contains counts (accumulated over 0.512 s) representing integral flux from the 10 electron detectors and 4 ion detectors. The time tag on each record marks the end of the 0.512 s accumulation interval. Each record also contains the counts for a 12 point energy spectrum from 1 ion detector. The timing for the differential ion data is identical to that of the integral ion and electron data. Counts for 14 point energy spectra from 2 electron detectors are included in each record. The accumulation interval for these spectra is 0.256 s; the first interval ends 0.128 s before the time tag, and the second ends 0.128 s after the time tag. The calibration procedure for conversion of decompressed counts to flux (both differential and

Table 13. Record structure of the EPAS header and data records.

Word	Description
	Header Record
1	Experiment ID (70152)
2	Year
3	Day of year
4	Orbit number
5	Start time of orbit (UT in milliseconds)
6	End time of orbit (UT in milliseconds)
7–18	Vacant (zero fill)
	Data Records
1	UT (milliseconds)
2	Compressed counts:
	Byte 1: Electron integral flux IDE0
	Byte 2: Electron integral flux IDE1
	Byte 3: Electron integral flux IDE2
	Byte 4: Electron integral flux IDE3
3	Byte 1: Electron integral flux IDE4
	Byte 2: Electron integral flux IDE5
	Byte 3: Electron integral flux IDE6
	Byte 4: Electron integral flux IDE7
4	Byte 1: Electron integral flux IDE8
	Byte 2: Electron integral flux IDE9
	Bytes 3–4: Vacant
5	Byte 1: Proton integral flux IDP0
	Byte 2: Proton integral flux IDP1
	Byte 3: Proton integral flux IDP2
	Byte 4: Proton integral flux IDP3
6	Byte 1: Sensor number for first electron spectrum
	Byte 2: Sensor number for second electron spectrum
	Byte 3: Sensor number for proton spectrum
	Byte 4: Vacant
7–13	Compressed counts (in byte form) for the first 14 point electron spectrum, followed by compressed counts (in byte form) for the second 14 point electron spectrum
14–16	Compressed counts (in byte form) for the 12 point proton spectrum

integral) is yet to be determined. Data for this sensor is acquired only while the spacecraft is operated in GTO telemetry mode.

The THDB files for EPAS consist of a header record followed by a series of data records. There is one data record per 0.512 s. Table 13 gives the record structure of the header and data records. Dummy fill (1 fill) is used for dropout within a spectrum. If dropout occurs for a full 0.512 seconds, resulting in loss of both electron spectra and the proton spectrum, no fill will take place. If dropout occurs such that the sensor number from which a spectrum is taken, is lost, the sensor number will be 1's filled.

The EPAS calibration file is in ASCII form and consists of a series of header records, comment records, electron energy channel records, electron geometric factor records, an proton geometric factor records. There is one information word per record. Table 14 contains the record structure of the calibration file.

Table 13. (Continued)

Word	Description
	Data Records
17	Byte 1: Compressed counts for proton coincidence counting rate Byte 2: Compressed counts for proton background counting rate Byte 3: Discrete information as follows: Bit 7: Telemetry dropout flag (1 if dropout occurred in the 0.512 s interval) Bit 6: C (calibration mode flag) Bit 5: K Bit 4: N Bit 3: S Bit 2: T Bit 1: W Bit 0: Telemetry flag: normally 0, set to 1 if a data gap follows due to a switch to CSM or LASSII telemetry mode. Byte 4: Vacant
18	Vacant

Table 14. EPAS Calibration file record structure.

Record	Description
	Header Records
1	Number of calibration files
2	Number of header records that follow (10) (I)
3	Experiment number (AFGL 701-5B) (CHAR*20)
4	Calibration file version number (I)
5	Valid start date for calibration (e.g. 89105) (I)
6	Valid end date for calibration (I)
7	Number of record types in calibration file (5) (I)
8	Number of comment records (I)
9	Number of electron energy channel records (I)
10	Number of electron geometric factor records (I)
11	Number of proton energy channel records
12	Number of proton geometric factor records (I)
	Comment Records
1–N	Comment records (CHAR*80)
	Electron Energy Channel Records (REAL)
1–14	E1 through E14 for electron detector 1
15–28	E1 through E14 for electron detector 2
⋮	⋮
127–140	E1 through E14 for electron detector 10
	Electron Geometric Factor Records (REAL)
1–14	G1 through G14 for electron detector 1
15–28	G1 through G14 for electron detector 2
⋮	⋮
127–140	G1 through G14 for electron detector 10
	Proton Energy Channel Records (REAL)
1–10	E1 through E10 for proton detector 1
⋮	⋮
31–40	E1 through E10 for proton detector 4
	Proton Geometric Factor Records (REAL)
1–10	G1 through G10 for proton detector 1
⋮	⋮
31–40	G1 through G10 for proton detector 4

3.2.5 Proton Telescope

The PROTEL telemetry consists of:

1. decompressed counts representing differential flux for a 24 point proton spectrum (1–100 MeV),
2. heavy ion dose in 10 channels (1.4–100 MeV),
3. 12 singles readouts from the high energy sensor head,
4. 9 singles readouts from the low energy sensor head,
5. command state bits and instrument bilevel and analog data.

The science data is acquired every 1.024 s. The data from the science words are extracted from the bit stream, decompressed into true counts, and stored in the THDB in 32 bit words. Thus one THDB data record represents 4.096 s. The THDB also includes the 8 command state bits and bilevels, designations B29 and B30 (SC-14, SF19 and SF20), and the 17 instruments analogs (designations A221–A237 located on SC11/SF15-31). The command state bits are used to determine periods when the instrument is in calibration mode. Analog A236 identifies the command state row. The remaining analog words are for instrument housekeeping data. The analogs and bilevels are stored in the THDB in their telemetry form (8 bit bytes) once per masterframe (4.096 s). The spectrum, dose, and singles data is sampled 1.024 s before being readout to telemetry. Data for this sensor is acquired in all spacecraft telemetry modes.

For the 24 proton channels, the conversion from true counts to differential flux is by means of a multiplicative constant (geometric factor) for each channel:

$$\text{DIFF FLUX(i)} = \text{PCOUNTS(i)} \times \text{GF(i)}\,,$$

where PCOUNTS(i) represents the decompressed counts for proton channel i, and GF(i) is the associated geometric factor.

The calibration procedure for the dose data is also by means of one multiplicative factor per channel:

$$\text{DOSE(i)} = \text{DCOUNTS(i)} \times \text{F(i)}\,,$$

where DCOUNTS(i) represents the decompressed counts for dose channel i, and F(i) is the associated multiplicative factor.

The PROTEL THDB files consist of a header record followed by a series of data records. Each data record is made up of data accumulated over a master frame (4.096 s). The header and data record structure is given in Table 15. The dropout

flag is set to 1 if there is dropout anywhere within the master frame. Dropout within a spectrum will be 1 filled.

The calibration file consists of ASCII data. The file contains a series of header records, comment records, energy value records, geometric factor records, and channel dependent constant records. There is one information word per record. The record structure of the calibration file is given in Table 16.

Table 15. Record structure of the PROTEL header and data records.

Word	Description
	Header Record
1	Experiment ID (70189)
2	Year
3	Day of year
4	Orbit number
5	Start time of orbit (UT in milliseconds)
6	End time of orbit (UT in milliseconds)
7–230	Vacant (zero fill)
	Data Records
1	UT (milliseconds)
2–9	Decompressed counts for the 8 LE differential proton spectra
10–25	Decompressed counts for the 16 HE differential proton spectra
26–35	Decompressed counts for the 10 heavy ion dose measurements
36–56	Decompressed counts for the LE singles channels (D1A, D12A, D123A, D134A, D5, D1, D2, D3, D4), followed by the HE singles channels (D1A, D12A, D123A, D134A, D145A, D6, Dr, D1, D2, D3, D4, D5)
57–111	Repeat the order of words 2–56 for the next 1.024 s.
112–166	Repeat the order of words 2–56 for the next 1.024 s.
167–221	Repeat the order of words 2–56 for the next 1.024 s.
222–226	Bilevels, analogs, and dropout flag in byte form in the order: B29, B30, A221–A237, dropout flag
227–230	Vacant

Table 16. PROTEL Calibration file record structure.

Record	Description
	Header Records
1	Number of calibration files
2	Number of header records that follow (9) (I)
3	Experiment number (AFGL 7018A) (CHAR*20)
4	Calibration version number (I)
5	Valid start date for calibration (e.g. 89105) (I)
6	Valid end date for calibration (I)
7	Number of record types in calibration file (5) (I)
8	Number of comment records (I)
9	Number of proton energy channel records (I)
10	Number of proton geometric factor records (I)
11	Number of dose threshold energy records
12	Number of dose calibration factor records (I)
	Comment Records
1–N	Comment records (CHAR*80)
	Proton Energy Channel Records (REAL)
1	LE E1
2	LE E2
⋮	⋮
8	LE E8
9	HE E1
10	HE E2
⋮	⋮
24	HE E16
	Proton Channel Geometric Factor Records (REAL)
1–8	LE Channel geometric factors
9–24	HE Channel geometric factors
	Dose Channel Energy Threshold Records (REAL)
1–10	Dose channel energy thresholds
	Dose Channel Calibration Constant Records (REAL)
1–10	Dose channel calibration constants

Table 17. Instrument modes for SEP.

Species	Mode	Energy Range	Channel Width
Electrons	ELEC1	20–300 keV	20 keV
	ELEC2	300–5000keV	400 keV
Protons	PROT1	0.5–4.5 MeV	330 keV
	PROT2	4.5–20 MeV	1.25 MeV
	PROT3	20–45 MeV	2.0 MeV
	PROT4	45–100 MeV	4.2 MeV

3.2.6 Spectrometer for Electrons and Protons

The SEP package consists of three sensors mounted at 80°, 60°, and 40° to the spacecraft spin axis. Each of the sensors is independently uplink commandable and is capable of providing electron spectra between 20–5000 keV or proton spectra between 0.5–100 MeV as 12 point differential flux spectra and 4 point integral flux readouts. Actual energy ranges selected in both electron and proton mode are commandable. Typical modes used during the CRRES mission are shown in Table 17. The sensors at 80° and 60° provide a full set of spectra every 0.256 s. The sensor at 40° produces the 12 spectrum points and 4 integral flux values every 0.512 s. The spectrum and integral flux data along with the status word information for all sensors are included in the THDB at the full data rate.

The THDB for SEP consist of a header record followed by a series of data records. The header record is in 32 bit positive integer form. There is one data record every 2 masterframes (8.192 s). Data values are in compressed counts. Data obtained during LASSII telemetry mode are stored in the THDB but may be unusable. For the LASSII periods, the LASSII flag is set to 'on' in the THDB. The word order of the spectra is as it is extracted from the telemetry stream and has not been reordered to be monotonic with respect to energy. The channel order is: 2, 4, 6, 8, 10, 12, 1, 3, 5, 7, 9, 11. The instrument mode must be determined from the status bits (bit numbering is 7 for the MSB and 0 for the LSB) as follows:

1. If the amplifier gain (LSB of the third status word) is 1, the data is electrons. If the bit is 0, the data is protons or α particles. In this case, if the D logic bit (bit 4 of the third status word) is 1 (for coincidence) and the PHA lower threshold (status word 5 of the six status words) is greater than 60 (decimal), then the data is α particles.

2. The current operating page number can be obtained from the 3 LSBs of the

first of the six status words.

3. The current operating mode number within the current page may be obtained from the 3 MSBs of the second of the six status words.

4. The PHA lower energy threshold can be obtained from the full 8 bit readout of the fourth of the six status words. Calibration data will be required to convert this value to energy.

5. The PHA upeer energy threshold can be obtained from the 6 MSBs of the fifth of the six status words. Calibration data are required to convert this value to energy.

Table 18 contains the record structure of the SEP header and data records. The calibration file structure is still to be determined.

3.2.7 Fluxgate Magnetometer

The magnetic field file consists of the millisecond time word, the 12 bit telemetered digital data corresponding to the X, Y, Z science magnetometer sensor outputs, the analog science magnetometer data, a temperature monitor, two 8 bit telemetry words containing bilevels, and the analog values from the spacecraft attitude magnetometers.

Universal Time (in milliseconds) is contained in a 32 bit word. The 12 bit digital data is in 2's complement form, with a range of -2048 to 2047, and are stored in 16 bit words. Bits 12 and 13 are designators identifying the sensor range. These variable gain outputs are written to the file tape at a rate of 8 times second. The low gain digital values are at a rate of 2 points per second. The high gain analog data are included at a rate of 4 points per masterframe; the low gain analogs occur once per masterframe. The temperature monitor and bilevel words occur once per masterframe. The magnetometer analogs, temperature monitor and bilevels are stored in their 8 bit telemetry form. The spacecraft X, Y, Z attitude magnetometers for both high gain and low gain are included in 8 bit analog form at their full rate of 4 points per masterframe. A flag bit is set to 1 whenever the spacecraft telemetry is in LASSII mode. Each record contains 16 master frames of data (approximately 65.536 s). Telemetry dropouts are 1's filled unless a full master frame is missing. Data from this sensor is not acquired during spacecraft LASSII telemetry mode.

The THDB files for the magnetometer consist of a header record followed by a series of data records. The header record is in 32 bit positive integer form. For the data records, all words are 32 bits: in the bit numbering sequence, bit 32 is the MSB of the 32 bit word, bit 1 is the LSB. Table 19 contains the header and data record structure. The format of the calibration file is yet to be determined.

Table 18. Record structure of the SEP header and data records.

Word	Description
	Header Record
1	Experiment ID (3073)
2	Year
3	Day of year
4	Orbit number
5	Start time of orbit (UT in milliseconds)
6	End time of orbit (UT in milliseconds)
7–330	Vacant (zero fill)
	Data Records
1	UT (milliseconds)
2	Bytes 1–4: First 4 SEPA status words for this masterframe
3	Bytes 1–2: Last 2 SEPA status words for this masterframe Bytes 3–4: Vacant
4	Vacant
5–7	1^{st} SEPA spectrum for this 4.096 s interval (data stored in consecutive bytes)
8–10	2^{nd} SEPA spectrum for this 4.096 s interval (data stored in consecutive bytes)
⋮	⋮
50–52	16^{th} SEPA spectrum for this 4.096 s interval (data stored in consecutive bytes)
53–56	16 values of integral flux 'DA' for this 4.096 s interval (data stored in byte form)
57–60	16 values of integral flux 'EA' for this 4.096 s interval (data stored in byte form)
61–62	8 values of integral flux 'AA' for this 4.096 s interval (data stored in byte form)
63–64	8 values of integral flux 'EPA' for this 4.096 s interval (data stored in byte form)
65–128	Repeat order of words 1–64 for the next 4.096 s interval containing the SEPA data
129–256	Repeat the order of words 1–128 for the 8.192 s interval for the SEPB data. With respect to the integral flux values, the DA, EA, AA, EPA values are replaced by DB, EB, AB, EPB, respectively.

Table 18. (Continued)

Word	Description
	Data Records
257	UT (milliseconds) at start of minor frame associated with the first SEPC spectrum (minor frame 4)
258	Bytes 1–4: First 4 SEPC status words for this masterframe
259	Bytes 1–2: Last 2 SEPC status words for this masterframe Bytes 3–4: Vacant
260	Vacant
261–263	1st SEPC spectrum for this 8.192 s interval (data stored in consecutive bytes)
264–266	2nd SEPC spectrum for this 8.192 s interval (data stored in consecutive bytes)
⋮	⋮
306–308	16th SEPC spectrum for this 8.192 s interval (data stored in consecutive bytes)
309–312	16 values of integral flux 'DC' for this 8.192 s interval (data stored in byte form)
313–316	16 values of integral flux 'EC' for this 8.192 s interval (data stored in byte form)
317–320	16 values of integral flux 'AC' for this 8.192 s interval (data stored in byte form)
321–324	16 values of integral flux 'EPC' for this 8.192 s interval (data stored in byte form)
325	Byte 1: Telemetry mode flag associated with the first of the 4.096 s time intervals (0=GTO, 1=LASSII) Byte 2: Telemetry mode flag associated with the second of the 4.096 s time intervals Byte 3: Telemetry dropout flag associated with the first of the 4.096 s time intervals (0: no dropout in the time interval, 1: dropout somewhere in the time interval) Byte 4: Telemetry dropout flag associated with the second of the 4.096 s time intervals
326–330	Vacant

Table 19. Record structure of the Fluxgate Magnetometer header and data records.

Header Record

Word	Description
1	Experiment ID (701131)
2	Year
3	Day of year
4	Orbit number
5	Start time of orbit (UT in milliseconds)
6	End time of orbit (UT in milliseconds)
7–1200	Vacant (zero fill)

Data Records

Word	Bits	Description
1	32–1	UT (milliseconds) at beginning of master frame
2	32–17	BXL(1)
	16–1	BYL(1)
3	32–17	BZL(1)
	16–1	BX(1)
4	32–17	BY(1)
	16–1	BZ(1)
5	32–17	BX(2)
	16–1	BY(2)
6	32–17	BZ(2)
	16–1	BX(3)
⋮	⋮	⋮
9	32–17	BZ(4)
	16–1	BXL(2)
10	32–17	BYL(2)
	16–1	BZL(2)
11	32–17	BX(5)
	16–1	BY(5)
⋮	⋮	⋮
16	32–17	BY(8)
	16–1	BZ(8)
17–32	Repeat order of words 1–16 for next second.	
33–48	Repeat order of words 1–16 for next second.	
49–64	Repeat order of words 1–16 for next second.	

Table 19. (Continued)

Data Records		
Word	Bits	Description
65	32–25	BXAL(1)
	24–17	BYAL(1)
	16–9	BZAL(1)
	8–1	BXA(1)
66	32–25	BYA(1)
	24–17	BZA(1)
	16–9	BXA(2)
	8–1	BYA(2)
67	32–25	BZA(2)
	24–17	BXA(3)
	16–9	BYA(3)
	8–1	BZA(3)
68	32–25	BXA(4)
	24–17	BYA(4)
	16–9	BZA(4)
	8–1	A241 (temperature 1B monitor)
69	32–25	B1
	24–17	B2
	16–9	B30
	8–1	Telemetry flag (0: GTO mode, 1: LASSII mode)
70	32–25	XSCH(1)
	24–17	XSCH(2)
	16–9	XSCH(3)
	8–1	XSCH(4)
71	32–25	YSCH(1)
	24–17	YSCH(2)
	16–9	YSCH(3)
	8–1	YSCH(4)
72	32–25	ZSCH(1)
	24–17	ZSCH(2)
	16–9	ZSCH(3)
	8–1	ZSCH(4)
73	32–25	XSCL(1)
	24–17	XSCL(2)
	16–9	XSCL(3)
	8–1	XSCL(4)

Table 19. (Continued)

Data Records		
Word	Bits	Description
74	32–25	YSCL(1)
	24–17	YSCL(2)
	16–9	YSCL(3)
	8–1	YSCL(4)
75	32–25	ZSCL(1)
	24–17	ZSCL(2)
	16–9	ZSCL(3)
	8–1	ZSCL(4)
76–150	Repeat order of words 1–75 for 2^{nd} master frame	
151–225	Repeat order of words 1–75 for 3^{rd} master frame	
⋮	⋮	
1126–1200	Repeat order of words 1–75 for 16^{th} master frame	

3.2.8 Ephemeris data

Spacecraft vectors are received at PLGD from the Consolidated Satellite Test Center (CSTC). These vectors along with magnetic field models are used as the prime input to the ephemeris generation routines. These routines are run prior to the Agency Tape generation.

Satellite ephemerides are generated routinely on the basis of regularly updated position-velocity vector sets provided by the CSTC. These vector sets are quality-checked for transmittal errors and stored chronologically in a file for use in ephemeris calculations. Position-velocity accuracy requirements are achieved through the use of an ephemeris code that includes the geopotentials that account for the significant perturbation from a Keplerian orbit. Availability of regular vector sets also eliminates the need for ephemeris prediction and will permit, instead, the use of reliable interpolation techniques. Inspection of incoming vector sets for consistency is integrated into the ephemeris processing system. When switching between vector sets, smoothing is performed to suppress any discontinuities of position which exceed a predetermined level.

In addition to generating satellite coordinates, the ephemeris system provides a data base containing solar and lunar coordinates, the geomagnetic field vector

and an event directory for eclipse and orbit adjust times. Solar and lunar position coordinates are computed and furnished as part of the standard ephemeris output. The following geomagnetic field parameters are also provided:

1. magnitude of field at vehicle location;
2. Earth Centred Inertial (ECI) components of magnetic field vector;
3. invariant latitude;
4. geographic location of 100 km intersection of vehicle's field line (both north and south hemispheres);
5. L-shell;
6. magnitude and location (latitude, longitude, altitude) of minimum field intensity along vehicle's field line;
7. geographic location of vehicle's conjugate point;
8. geomagnetic local time (MLT) in hours, given by

$$\mathrm{MLT} = \frac{\mathrm{ML_{sat}} - \mathrm{ML_{\odot}}}{15} + 12\,,$$

where $\mathrm{ML_{sat}}$ and $\mathrm{ML_{\odot}}$ represent the geomagnetic longitude of, respectively, the vehicle and of the Sun at the time of interest.

The geomagnetic field is computed by means of the IGRF 85 internal field model and the Olson-Pfitzer external field model (Olson & Pfitzer 1977).

Ephemeris data files are replicas of the files placed on the Agency Tapes. Data records are in 32 bit positive integer form (31 data bits and the MSB set equal to 0). Offset and bias values are provided to convert the positive integer values to true units. For altitudes less than $3\,\mathrm{R_E}$, the data rate is once per minute. For higher altitudes, the data rate is once per 5 minutes.

To convert the 32 bit positive integer data to proper units (e.g. km), subtract 2^{30} from the THDB value and then multiply by the appropriate factor. All factors are given as powers of 10 in the THDB. Thus, to convert WORD(i) to physical units [PHYSUNIT(i)], apply the expression

$$\mathrm{PHYSUNIT(i)} = \left[\mathrm{WORD(i)} - 2^{30}\right] \times 10^{\mathrm{FACTOR(i)}}\,.$$

Table 20 gives a description of the record structure of the ephemeris files and also lists the appropriate multiplicative factors as powers of 10.

Table 20. Record structure of the ephemeris files. The multiplicative factors in the third column are given as powers of 10.

Word	Description	Factor
1	Day number (days)	0
2	UT (milliseconds)	0
3	X, Satellite position, ECI[1] (km)	−4
4	Y, Satellite position, ECI (km)	−4
5	Z, Satellite position, ECI (km)	−4
6	VX, Satellite velocity, ECI (km/s)	−7
7	VY, Satellite velocity, ECI (km/s)	−7
8	VZ, Satellite velocity, ECI (km/s)	−7
9	Radius, Earth centre to satellite (km)	−4
10	Altitude (km)	−4
11	Latitude (deg)	−6
12	Longitude (deg)	−6
13	Velocity (km/s)	−7
14	Local Time (hr)	−7
15	Radius, MAG[2] (EMR[3])	−7
16	Latitude, MAG (deg)	−6
17	Longitude, MAG (deg)	−6
18	Radius, SM[4] (EMR)	−7
19	Latitude, SM (deg)	−6
20	Local Time, SM (hr)	−7
21	Radius, GSM[5] (EMR)	−7
22	Latitude, GSM (deg)	−6
23	Local Time, GSM (hr)	−7
24	B (nT)	−4
25	BX, ECI (nT)	−4
26	BY, ECI (nT)	−4
27	BZ, ECI (nT)	−4
28	Magnetic Local Time (hr)	−7
29	Solar zenith angle (deg)	−6
30	Invariant latitude (deg)	−6
31	B100N Latitude (deg)	−6
32	B100N Longitude (deg)	−6
33	B100S Latitude (deg)	−6
34	B100S Longitude (deg)	−6

Table 20. (Continued)

Word	Description	Factor
35	L-shell (EMR)	−7
36	BMIN (nT)	−4
37	BMIN Latitude (deg)	−6
38	BMIN Longitude (deg)	−6
39	BMIN Altitude (km)	−4
40	BCONJ Latitude (deg)	−6
41	BCONJ Longitude (deg)	−6
42	BCONJ Altitude (km)	−4
43	X Sun Position, ECI (km)	0
44	Y Sun Position, ECI (km)	0
45	Z Sun Position, ECI (km)	0
46	X Moon Position, ECI (km)	0
47	Y Moon Position, ECI (km)	0
48	Z Moon Position, ECI (km)	0
49	Right Ascension of Greenwich	−6
50	B100N Magnetic Field (nT)	−4
51	B100S Magnetic Field (nT)	−4
52	MX Dipole Moment, ECI (nT)	−4
53	MY Dipole Moment, ECI (nT)	−4
54	MZ Dipole Moment, ECI (nT)	−4
55	DX Dipole Offset, ECI (km)	−4
56	DY Dipole Offset, ECI (km)	−4
57	DZ Dipole Offset, ECI (km)	−4
58–60	Vacant	

[1]ECI: Earth Centred Inertial Coordinates
[2]MAG: Magnetic Coordinates
[3]EMR: Earth Mean Radius (6371.2 km)
Equatorial radius is defined as 6378.135 km, flattening as 298.26.
[4]SM: Solar Magnetic Coordinates
[5]GSM: Geocentric Solar Magnetospheric Coordinates

3.2.9 Attitude determination data

The CRRES attitude determination subsystem is used to determine the spacecraft attitude and spin rate. This allows subsystems to keep within nominal environments, and provides a reference frame for science data. The attitude determination subsystem is designed to provide knowledge of the CRRES spin axis in inertial space, to within $\pm 2.0°$, $1\,\sigma$.

The experimenter's requirement to know the instruments' line-of-sight as a function of time throughout the orbit is met by processing Sun sensor, Earth horizon sensor and spacecraft magnetometer output along with vehicle ephemeris data through an attitude determination program to calculate the vehicle spin axis in ECI coordinates together with the spin phase and spin rate. These data are used to calculate coefficients of functions over segments of the orbit which are written on a file on the agency tape. A software module provided to each experimenter reads these coefficients and calculates the sensor line-of-sight for the designated time. Fitting procedures insure that results are continuous over segment boundaries. The attitude coefficient THDB file is identical to the attitude coefficient file stored on the agency tapes.

The attitude coefficient file contains the output of the attitude determination program. Data records are in ASCII. The data consist of a series of time tagged coefficients from fits of attitude motion. This file is used in conjunction with software (program AGMOD) provided to the agencies to calculate sensor line of sight as a function of time. The file structure consists of an information header followed by the fit coefficient data, and is listed in Table 21.

3.3 Final data sets

In order to derive physical quantities from the THDB files for the particle instruments for a given orbit, their respective THDB files have to be combined with the corresponding ephemeris files, attitude determination files, and the magnetometer THDB files. For the determination of pitch angles, the direction of the line of sight of the instruments also has to be calculated. Furthermore, the exact time of the measurements in different channels needs to be determined.

One problem with the data is the intermittent availability of magnetometer data, required for computing the real pitch angle. For times when magnetometer data are unavailable, model pitch angle data must be used. For example, there are no magnetometer data from orbits 366 to 409. It is possible that some of this will be 'restored' at a later date.

After consultation with D. Brautigam and M. Violet at PLGD, it was suggested that HEEF and PROTEL data could be provided in a format already containing

Table 21. File structure of the attitude coefficient files.

Word	Description	Word Type
	Header Information	
1	File name	Alpha
2	Vehicle ID	Alpha
3	GTO (LASSII) Period number	Alpha
4	Year	Integer
5	Day of year	Integer
6	UT at start of data (ms)	Integer
7	UT at end of data (ms)	Integer
8	Number of fit spans	Integer
	Fit Coefficient Records	
1	Index (state vector) number	Integer
2	Segment start time (sec)	Floating
3	Segment end time (sec)	Floating
4	Time conversion scale factor	Floating
5	Time conversion offset factor	Floating
6	Condition flag number	Integer
7	Order of RA fit coefficient (N1)	Integer
8	Spin axis RA fit coefficient 1	Floating
9	Spin axis RA fit coefficient 2	Floating
⋮	⋮	⋮
7+N1	Spin axis RA fit coefficient N1	Floating
8+N1	Order of DEC fit coefficient (N2)	Integer
9+N1	Spin axis DEC fit coefficient 1	Floating
10+N1	Spin axis DEC fit coefficient 2	Floating
⋮	⋮	⋮
8+N1+N2	Spin axis DEC fit coefficient N2	Floating
9+N1+N2	Order of spin rate fit coefficient (N3)	Integer
10+N1+N2	Spin rate fit coefficient 1	Floating
11+N1+N2	Spin rate fit coefficient 2	Floating
⋮	⋮	⋮
9+N1+N2+N3	Spin rate fit coefficient N3	Floating
10+N1+N2+N3	Spin phase at start of segment	Floating

pitch angles and the correct measurement timings. An additional advantage of this approach would be a significant reduction in the size of the final data sets. For instance, the complete THDB for PROTEL comprises about 8 Gb, which could be compressed by a factor 3 or more when transformed into the format containing pitch angles, and even further when a binary format is used.

Spare instruments for HEEF and PROTEL are being re-calibrated and new calibrations will be applied to the data in a 6–12 month timescale. Final data will not be released until this process is completed.

The cross-calibrations of the electron instruments HEEF, MEES and EPAS are in a well-advanced stage. At high altitudes and away from the magnetic equatorial plane, the overlap agreement among the three instruments is excellent. However, at lower altitudes and closer to the magnetic equatorial plane, the overlap between HEEF and MEES is not good. Mullen and Gussenhoven (1991) concluded that electrons with energy greater than 2 MeV can contaminate both of the medium energy electron sensors, MEES and EPAS. Corrections for the contamination are still being prepared and must be made if data from these instruments are to be used for regions with substantial high energy particle populations. The HEEF data are remarkably contamination-free except at the inner edge of the inner radiation belt where the highest energy protons are trapped. Here some subtraction will be necessary, the exact level still to be determined.

3.3.1 Preliminary PROTEL data

As a result of visits to PLGD, a preliminary batch of high-resolution PROTEL data, comprising orbits 411–420, was sent by PLGD to ESTEC. These orbits were chosen because they represent a quiet time when low L-values were reasonably well covered, since one of our first tasks is to examine the low-altitude part of the data. Although the data will be subject to later re-calibration, they should allow data analysis procedures to be developed and problems to be ironed out.

The data are provided as counts in function of universal time, L-shell, and pitch angle. The time resolution is one second. This means that, taking into account the spin rate of 2 rpm, the pitch angle resolution is at best 12°.

There is one data file per orbit. The files are in ASCII format and contain eight header records and a series of data records. The header records contain the orbit number, the date of the start of the orbit, the beginning and ending times (UT) of the orbit, the minimum and maximum L-shell, and the first and last energy channel number. The data records consist of the year, day number, UT (in seconds), L-shell (in R_E), pitch angle, and counts for the 16 HEH channels. The Fortran format of a data record is

(i2, i4, f8.1, f5.2, f5.0, 16i7)

PLGD also provided the code for three Fortran functions to calculate the average energy of a channel, the conversion factors to differential flux, and the distribution function:

1. PROENG(J): returns the average energy of the channel in Mev. J is the channel number (1–24).
2. PROFLUX(J): returns the conversion constant to differential flux of the channel in units of $(\mathrm{cm}^2\,\mathrm{s\,sr\,Mev})^{-1}$:

$$\mathrm{FLUX(J)} = \mathrm{COUNT(J)} \times \mathrm{PROFLUX(J)}\,.$$

3. PRODIST(J): same as PROFLUX(J), but only for the distribution function.

3.3.2 Custom PLGD databases and software

Software has been developed at PLGD to average particle data over L- and pitch angle-bins. However, we think it to be more appropriate to transfer the data at full spatial and pitch angle resolution. PLGD also defined a fluence as the summation of the L-binned fluxes over pitch angle. Although the sizes of the data sets are substantially reduced in this way, directional information is completely lost, so that mirror-point distributions or extrapolations along field lines can no longer be retrieved.

PLGD have also developed a number of intermediate custom databases and display systems for their own purposes, including the "FLUENCE" system. This software package is used to visualize data and contains the following routines:

1. SSDB graphics;
2. DIPOLE DOSE;
3. LEPA applications (not installed);
4. CRRES particle data:
   - HE program,
   - FLUENCE program,
   - DOSE program,
   - DMSP program,
   - RPD flux program.

DIPOLE DOSE program

This routine displays dosimeter data in geomagnetic R, λ coordinates, computed using an internal and external field model. Separate dosimeter channels are displayed: LOLET, HILET, and Stars, for all the dosimeter dome thicknesses. The CRRES mission is divided into three periods: quiet (before March 1991), disturbed (later than March 1991) and complete mission, for averaging. Derived fluences and radiation belt models are also displayed.

HE program

This custom program (by D. Brautigam) allows PROTEL, HEEF and MEA data to be read in and displayed simultaneously for inter-comparison. Data are organized in L-bins of $1/20\, R_{\mathrm{E}}$. Both electron spectra (HEEF with MEA superimposed) and PROTEL proton spectra are displayed, the point of interest being selected interactively from the flux-time plot.

FLUENCE program

This program displays data from the complete mission or a sub-set as colour-coded omnidirectional fluxes plotted in an L vs. orbit number panel. All 24 PROTEL channels and 10 HEEF channels are available.

DOSE program

This program is similar to FLUENCE but provides all 24 dosimeter channels.

Chapter 4

Preliminary results from the CRRES mission

Although the calibration process for the most of the CRRES instruments is still going on, some results and conclusions have already been derived from the preliminary data. These preliminary results include:

1. a comparison of magnetic field models with CRRES magnetometer data;
2. an investigation into the dynamics of the radiation belts, with emphasis on the major solar proton event of 23–31 March 1991, and the ensuing Sudden Storm Commencement (SSC);
3. development of a quasi-static model of outer-zone electrons;
4. development of radiation dose models;
5. a comparison of CRRES particle detector data with existing NASA radiation belt models;
6. location of the South Atlantic Anomaly (SAA).

The first four studies were carried out at PLGD. In the following sections, we present a summary of the results. The last two studies were made with the SSDB and are discussed in Sect. 3.1.3 and 3.1.4.

4.1 Magnetic field models

Jordan & Bass (1990), Bass & Jordan (1990) and Jordan et al. (1992) have made a comprehensive study of the available magnetospheric internal and external magnetic

field models in the context of the CRRES data analysis. These authors compared model predictions of the geomagnetic field to CRRES magnetometer measurements.

The internal field models investigated are: IGRF 1985, a model developed by Cain et al. (1989) to describe a discontinuity in the secular variation of the geomagnetic field in 1983 (Cain 1987), and the model developed by Barraclough et al. (1975). It was found that the differences between IGRF 1985 and the Cain model are not significant with respect to the calculation of L. In any case, the anomalous secular variation of the field is incorporated in later versions of the IGRF models, i.e. DGRF 1985 and IGRF 1990, which should thus be used.

Several models have been developed to describe the external contribution to the geomagnetic field. For the problem of sorting the CRRES data to create new radiation belt models, empirical or semi-empirical models are better suited than simple analytical models and complex magnetohydrodynamic models. All the models in the comparison study are of this first kind. Except for the Mead-Fairfield model (Mead & Fairfield 1975), they all start with a description of three basic current systems (magnetopause current, ring current and tail currents), determine the contributions of each current system to the magnetic field, and sum them to find the total contribution of the external field sources to the magnetic field.

The comparative study comprised the following models: Mead-Fairfield (Mead & Fairfield 1975), Olson-Pfitzer tilt dependent (Olson & Pfitzer 1977), Olson-Pfitzer dynamic (Pfitzer et al. 1988), Tsyganenko-Usmanov (Tsyganenko & Usmanov 1982), Tsyganenko (1987), Tsyganenko (1989), Stern parabolic magnetopause–stretched magnetosphere (Stern 1985, 1987), and Hilmer-Voigt (Hilmer 1989). Although it is very difficult to select a single model that is optimal over all regions and all levels of activity of the magnetosphere, the Olson-Pfitzer dynamic model was recommended for use with analysis of CRRES data. This model is easy to use provided the stand-off distance and either D_{st} or K_p are available. It is fast enough for extensive computations, and is well suited for analysis of large data sets where the large scale dynamic shifts are of interest.

R. Liu of MSSL applied the Tsyganenko 89 model to CRRES data. There are large discrepancies between the model field and the measured field at very low L-values. The Tsyganenko 87 model was modified to include a scaling factor, which is a function of the D_{st} index, on the ring-current contribution. The resulting field model is in better agreement with the measured field than the model field used for the SSDB. A magnetic field line tracing program, using the Tsyganenko 87 external field model, has been implemented. The program traces the field line through a specified point down to any desired height above the Earth's surface. A program to calculate field line integrals, using the field line tracing program, is being developed.

4.2 Double-peaked inner radiation belt

Existing inner proton belt models show a singly-peaked proton population which was thought to change very little. Early inner belt proton data measured by McIlwain (1963) showed the first evidence of a more complicated structure, namely a second peak. Using dosimeter data from the Defense Meteorological Satellite Program (DMSP) F7 Spacecraft, the second belt was again detected starting in February 1986 (Gussenhoven et al. 1989). However, in both instances the data were dismissed by the modeling community and never considered in the development of the inner belt proton models.

Mullen et al. (1991) used data from PROTEL and MEP to study the formation and stability of the double-peaked inner proton belt. The data are centred around the major solar proton event of 23–31 March 1991. The proton event was associated with a flare which began at 22:42 UT on 22 March, and was classified as Importance 3 in brilliance. At 03:42 UT on 24 March an extremely large SSC was recorded, indicating a high intensity solar wind shock hitting the magnetosphere at this time.

At the time when the shock hit, a peak was measured in the high energy PROTEL channels. The channels above approximately 20 MeV showed the largest increases in intensity. On the next orbit, the effects of the solar proton event and SSC can be seen extending all the way down into the inner belt region where a second belt above the steady-state inner belt was in its formative stage. Once formed, the belt remains in a stable state for a long period. It has not yet been determined exactly how long the protons remain stably trapped in the second belt.

The effect of the double belt structure are also very evident in single event upset rates between L-shells of 1.8 and 2.5. The increased upset rates can have a major impact on spacecraft operating in or through this region of space.

The empirical NASA AP-8 inner radiation belt proton models clearly are incapable of predicting the events evidenced by the CRRES measurements. The energetic inner belt proton region can extend to higher altitudes than given by the NASA model and can form a double-peaked structure following large solar shocks associated with solar proton events. Once injected, the higher altitude protons become stably trapped and remain for weeks to months. These results need to be incorporated in new inner belt proton models. Since these events occur infrequently, they will have to be treated in terms of the probability that a large shock occur and produce a second belt. In addition, the time decay of the second proton belt will also have to be included.

The cosmic ray cutoff models used to determine regions where normal cosmic ray backgrounds and solar protons affect satellite systems may also need to be revised. The CRRES data indicate that for particles in the energy range that produce SEUs

in electronic components, the rigidity cutoffs predicted by currently used models are incorrect. The cutoff altitudes are too high both for solar protons that enter the magnetosphere prior to shock and for the shock-associated particles that penetrate much further into the magnetosphere. Even galactic cosmic ray particles that create SEUs penetrate much further into the magnetosphere than the models predict.

4.3 Quasi-static model of outer-zone electrons

The outer-zone relativistic electron population has up to now been modeled by the static NASA solar minimum and maximum models AE-8 MIN and AE-8 MAX. In order to provide a more suitable description of this highly dynamic environment, a quasi-static model of the outer zone electrons was developed (Brautigam et al. 1992).

The database for this modeling project was generated from 30 s (1 spin) average HEEF fluxes, accumulated in L-shell bins of $0.2\,R_{\mathrm{E}}$ over the outer belt region from 2.4 to $6.6\,R_{\mathrm{E}}$. The data in each bin was then averaged to obtain a daily flux value in function of L for each energy channel.

For an individual flux profile, i.e. electron flux vs. L, for a given energy channel, two parameters P_1 and P_2 are defined. P_1, the *profile flux* parameter, is the integral of the flux over L:

$$P_1(E) = \sum_{i=1}^{21} j_i(E)\,\Delta L_i\,,$$

where i is the L-bin number (1 to 21), L_i the midpoint of L-shell i in R_{E} (2.5–$6.5\,R_{\mathrm{E}}$), $\Delta L = 0.2\,R_{\mathrm{E}}$ the width of an L-bin, and $j_i(E)$ the flux in L-bin i for a given energy channel (E). P_1 is a measure of the flux intensity in the outer zone. P_2, the *centroid* L parameter, is defined as

$$P_2(E) = \frac{\sum_{i=1}^{21} L_i\, j_i(E)\,\Delta L_i}{\sum_{i=1}^{21} j_i(E)\,\Delta L_i}\,,$$

and indicates the centre of the flux distribution.

P_1 and P_2 were calculated for electron flux profiles for each day of the CRRES mission and for each HEEF energy channel. It was then found that there is a moderate correlation between these two flux profile parameters and the 15 day running average $A_{\mathrm{p}15}$ of the A_{p} magnetic activity index. Therefore, $A_{\mathrm{p}15}$ was used to separate and bin the electron data to produce the new flux models.

Because of the highly dynamic nature of the outer belt electrons, the development and use of a single model to reproduce all conditions is not practical. It was

concluded that 8 models divided over the CRRES A_{p15} range between 5 and 55 nT would give a good representation of most conditions measured on CRRES. All daily flux profiles corresponding to the days assigned to one of the 8 A_{p15} intervals (assuming a 1 day lag time between flux and A_p) were averaged together to determine the model profile for that activity level.

Of the resulting 8 model profiles, the 2 profiles corresponding to the periods of lowest magnetic activity are significantly different in shape and magnitude from the remaining higher activity profiles. The higher activity profiles are themselves very similar in both shape and magnitude.

The 8 model flux profiles were compared with the single flux profile for the static model AE-8 MAX. In all energy channels the NASA model gives values higher than the CRRES models for $L > 5\,R_E$. For energies above about 2 MeV, the NASA model gives higher values at $L >\sim 3.4\,R_E$.

The new quasi-static model in the form of 8 flux profiles keyed to the magnetic activity index A_p, provides a more accurate representation of the dynamic outer zone electron environment than could be expected from any static model.

4.4 Development of radiation dose models

Three dose models were constructed using direct measurements of dose on the CRRES satellite (Gussenhoven et al. 1992). The quiet model uses data taken before the March 1991 storm, the active model is based on data taken after this event, and the average model uses data over the entire 14 months of the CRRES mission. Each model contains HILET and LOLET dose for the four different aluminium shielding thicknesses.

The models were created by accumulating the dose measurements in L- and B/B_0-bins for each orbit by channel. The data from all orbits appropriate to a given model were then combined by performing a simple average over all measurements falling into each L,B/B_0 bin. The data were then corrected for the onboard α source.

When the models are averaged for the three B/B_0 values closest to the magnetic equator and plotted as a function of L, several differences between the quiet and active models become apparent. In the quiet model, there is a clear slot region between 2 and 3 R_E, separating the inner and outer radiation belts. The slot region in the active model is filled with new HILET and LOLET belts, comparable in peak intensity with the inner belt. In addition, the active outer belt is more intense than the quiet one. The inner belt is unchanged in the two models.

A software package (CRRESRAD) was developed at PLGD to estimate directly the dose encountered by satellites in low inclination orbits. With this software, a comparison was made between active and quiet conditions for several circular, 0°

inclination orbits, at 1.55, 2.20, 2.50, 3.50, and 6.60 R_E, respectively. The dose in the inner belt region is the same for both models. The dose in the slot region increases by a factor of 30 to 100, depending on shielding thickness. At the outer edge of the newly formed belt at 2.5 R_E, the dose is still approximately 50 times higher than the pre-event level. The dose in the outer belt changes by about a factor of 10 on the average, while the dose increases at geosynchronous altitude are small. From this comparison, it is clear that radiation belt dynamics must be considered in mission planning, particularly for satellites travelling mainly in the slot region.

4.5 Relative position of CRRES and Meteosat

A program was developed by N. Flowers of MSSL to animate the relative position of CRRES to Meteosat. The program currently monitors the proximity of the satellites in kilometers, and will be extended to the use of L-shells.

The screen display shows the orbit of CRRES relative to a fixed Earth and Meteosat. There are views in the plane of the Meteosat orbit, and perpendicular to it.

Two windows display the following data for the two satellites: orbit number, longitude, latitude, radius, time, and date for CRRES, and longitude, latitude, CRRES distance, and date for Meteosat. A third window displays current universal time and Julian date. A fourth window can list out close approaches of the two satellites for a radially or vertically specified range. The fifth window shows the user options.

Eventually, it is intended to add a display of particle data for each point in the data files.

References

Barraclough, D.R., Harwood, J.M., Leaton, B.R., Malin, S.R.C.: 1975, *A Model of the Geomagnetic Field at Epoch 1975*, Geophys. J. R. Astr. Soc. **43**, 645–659

Bass, J.N., Jordan, C.E.: 1990, *Models of the External Source Contribution to Magnetospheric Magnetic Fields for CRRES Data Analysis*, GL-TR-90-0009

Blake, J.B., Imamoto, S.S.: 1992, *Proton Switches*, Journal of Spacecraft and Rockets **29**, 595–596

Brautigam, D.H., Gussenhoven, M.S., Mullen, E.G.: 1992, *Quasi-Static Model of Outer Zone Electrons*, submitted for publication in IEEE Transactions on Nuclear Science

Cain, J.C.: 1987, Private Communication to C.E. Jordan and J.N. Bass

Cain, J.C., Wang, Z., Kluth, C., Schmitz, D.R.: 1989, *Derivation of a Geomagnetic Model to* $n = 63$, Geophys. J. **97**, 431–441

CRRES System Description Handbook, Rev. E, Ball Aerospace Systems Division, Boulder, CO, 1990

Delorey, D.E.: 1991, *Combined Release and Radiation Effects Satellite Time History Data Base*, PL-TR-91-2140

Griffin, A.R., Delorey, D.E., MacInerney, R.E.: 1989, *CRRES Agency Tape Generation*, GL Technical Memorandum No. 174

Gussenhoven, M.S., Mullen, E.G., Sagalyn, R.C.: 1985, *CRRES/SPACERAD Experiment Descriptions*, AFGL-TR-85-0017

Gussenhoven, M.S., Mullen, E.G., Holeman, E.: 1989, *Radiation Belt Dynamics During Solar Minimum*, IEEE Transactions on Nuclear Science **36**, 2008–2014

Gussenhoven, M.S., Mullen, E.G., Sperry, M., Kerns, K.J.: 1992, *The Effect of the March 1991 Storm on Accumulated Dose for Selected Satellite Orbits: CRRES Dose Models*, submitted for publication in IEEE Transactions on Nuclear Science

Gussenhoven, M.S., Sperry, M.: 1992, *Private Communication*

Heck, F.: 1992, *Observation of Radiation Environment with CRRES Data*, ESTEC Stage Report

Hilmer, R.V.: 1989, *A Magnetospheric Magnetic Field Model with Flexible Internal Current Systems*, Ph. D. Thesis, Rice Univ., Houston, Texas

Jordan, C.E.: 1989, *NASA Radiation Belt Models AP-8 and AE-8*, GL-TR-89-0267

Jordan, C.E., Bass, J.N.: 1990, *Evaluation of Magnetospheric Internal Magnetic Field Models and Existing Software*, GL-TR-90-0014

Jordan, C.E., Bass, J.N., Gussenhoven, M.S., Singer, H.J., Hilmer, R.V.: 1992, *Comparison of Magnetospheric Magnetic Field Models with CRRES Observations During the August 26, 1990, Storm*, J. Geophys. Res. **97**, 16907–16920

Korth, A., Kremser, G., Wilken, B., Güttler, W., Ullaland, S.L., Koga, R.: 1992, *Electron and Proton Wide-Angle Spectrometer (EPAS) on the CRRES Spacecraft*, Journal of Spacecraft and Rockets **29**, 609–614

Lemaire, J., Daly, E.J., Vette, J.I., McIlwain, C.E., McKenna-Lawlor, S.: 1990, *Secular Variations in the Geomagnetic Field and Calculations of Future Low Altitude Radiation Environments*, Proceedings of the ESA Workshop on Space Environment Analysis, 9–12 October 1990, ESTEC, Noordwijk, The Netherlands, ESA WPP-23

McIlwain, C.E.: 1961, *Coordinates for Mapping the Distribution of Magnetically Trapped Particles*, J. Geophys. Res. **66**, 3681–3691

McIlwain, C.E.: 1963, *The Radiation Belts, Natural and Artificial*, Science **142**, 355–361

Mead, G.D., Fairfield, D.H.: 1975, *A Quantitative Magnetospheric Model Derived from Spacecraft Magnetometer Data*, J. Geophys. Res. **80**, 523–534

Mullen, E.G., Gussenhoven, M.S.: 1991, *Results of Space Experiments: CRRES*, PLGD Internal Report

Mullen, E.G., Gussenhoven, M.S., Ray, K., Violet, M.: 1991, *A Double-Peaked Inner Radiation Belt: Cause and Effect as Seen on CRRES*, IEEE Transactions on Nuclear Science **38**, 1713–1717

Olson, W.P., Pfitzer, K.A.: 1977, *Magnetospheric Magnetic Field Modeling*, Annual Scientific Report, AFOSR Contract No. F44620-75-C-0033, McDonnell Douglas Astronautics Company, Huntington Beach, CA

Pfitzer, K.A., Olson, W.P., Mogstad, T.: 1988, *A Time Dependent, Source Driven Magnetospheric Magnetic Field Model*, EOS **69**, 426

Stern, D.P.: 1985, *Parabolic Harmonics in Magnetospheric Modeling: The Main Dipole and the Ring Current*, J. Geophys. Res. **90**, 10851–10863

Stern, D.P.: 1987, *Tail Modeling in a Stretched Magnetosphere 1. Methods and Transformations*, J. Geophys. Res. **92**, 4437–4448

Tsyganenko, N.A.: 1987, *Global Quantitative Models of the Geomagnetic Field in the Cislunar Magnetosphere for Different Disturbance Levels*, Planet. Space Sci. **35**, 1347–1358

Tsyganenko, N.A.: 1989, *A Magnetospheric Magnetic Field Model with a Warped Tail Current Sheet*, Planet. Space Sci. **37**, 5–20

Tsyganenko, N.A., Usmanov, A.V.: 1982, *Determination of the Magnetospheric Current System Parameters and Development of Experimental Geomagnetic Field Models Based on Data from IMP and HEOS Satellites*, Planet. Space Sci. **30**, 985–998

Vampola, A.L., Osborn, J.V., Johnson, B.M.: 1992, *CRRES Magnetic Electron Spectrometer AFGL-701-5A (MEA)*, Journal of Spacecraft and Rockets **29**, 592–595

Vette, J.I.: 1991, *The NASA/National Space Science Data Center Trapped Radiation Environment Model Program*, NSSDC/WDC-A-R&S 91-29

Violet, M.D., Lynch, K., Redus, R., Riehl, K., Boughan, E., Hein, C.: 1992, *The Proton Telescope (PROTEL) on the CRRES Spacecraft*, IEEE Transactions on Nuclear Science, in press